High-Resolution Monte-Carlo Simulation of Flow and Conservative Transport in Heterogeneous Porous Media: 1, Methodology and Flow Results

R.L. Naff

U.S. Geological Survey

Water Resources Division

Denver, Colorado, USA

D.F. Haley

Waterloo Centre for Groundwater Research

University of Waterloo

Waterloo, Ontario, Canada

E. A. Sudicky

Waterloo Centre for Groundwater Research

University of Waterloo

Waterloo, Ontario, Canada

August, 1996

Revised June, 1997

Abstract

In this first of two papers concerned with the use of numerical simulation to examine flow and transport parameters in heterogeneous porous media via Monte-Carlo methods, various aspects of the modelling effort are examined. In particular, the need to save on core memory causes one to use only specific realizations that have certain initial characteristics; in effect, these transport simulations are conditioned by these characteristics. Also, the need to independently estimate length scales for the generated fields is discussed. The statistical uniformity of the flow field is investigated by plotting the variance of the seepage velocity for vector components in the x, y and z directions. Finally, specific features of the velocity field itself are illuminated in this first paper. In particular, these data give one the opportunity to investigate the effective hydraulic conductivity in a flow field which is approximately statistically uniform; comparisons are made with first- and second-order perturbation analyses. The mean cloud velocity is examined to ascertain whether it is identical to the mean seepage velocity of the model. Finally, the variance in the cloud centroid velocity is examined for the effect of source size and differing strengths of local transverse dispersion.

Introduction

As large, high-speed computing facilities become more readily available the feasibility of doing Monte-Carlo (MC) simulations of three-dimensional flow and transport in heterogeneous porous media becomes more apparent. This report and its companion paper is a compendium of our experience with MC simulations of flow and transport within a large, finely discretized domain. The problem that we attempt to emulate is the migration of a conservative tracer in a heterogeneous clastic aquifer under natural gradient conditions. That is, a heterogeneous medium causes the flow field to be randomly nonuniform and results in the enhanced dispersion of a tracer. The effect of a heterogeneous medium on the flow field is simulated by modelling flow through a hydraulic conductivity field generated from a second-order stationary process; other sources of variability to the flow field are ignored. By varying the statistical makeup of the hydraulic conductivity field, one can examine the effects of statistical anisotropy and variance in the hydraulic conductivity on the mean flow and transport phenomena. This problem has been critically examined in the literature using first-order analytical procedures [e.g., *Dagan*, 1982, 1984, 1988, 1990, 1991; *Gelhar and Axness*, 1983], allowing for comparisons with the results of this effort.

We elected, in these simulations, to use only conservative tracers; in part this choice reflects the current lack of knowledge concerning the spatial statistics of reactive parameters; however, we also consider that many questions concerning the transport of non-reactive tracers remain unanswered or only partially answered. Even though the platform on which these models were run (a Cray-3 supercomputer made available through the National Center for Atmospheric Research) was, with regard to memory, a relatively large machine, limitations on domain size were still a factor. Critical to the solution of the transport problem was the mesh size; the domain discretizations had to be sufficiently fine to eliminate most oscillation in the solution to the concentration field. This requirement

had to be balanced with a desire to make the domain sufficiently large so that the large time moments could be obtained. Time stepping in the solution of the transport processes was avoided by solving for the concentration field in Laplace space and then only inverting for the desired range of times.

Numerical simulation of heterogeneous porous media has basically followed two trends. One trend, as exemplified by *Jussel et al.* [1994a, 1994b] and *Webb and Anderson* [1996] is to depict, as accurately as possible, the medium in a geologic context; that is, should the environment of deposition require the presence of certain features, then the emphasis is to create a medium generation scheme whereby those features are preserved. The other trend, as exemplified by *Tompson and Gelhar* [1990], *Tompson* [1993], *Chin and Wang* [1992] and *Bellin et al.* [1992] is more engineering oriented in that the emphasis is on representing the medium as parsimoniously as possible; this is usually accomplished by assuming an autocovariance representation for the hydraulic conductivity field and then basing the generation scheme on this particular correlation structure. This approach has the advantage that, should the representation be appropriate, then the medium at any site could be quantified by intensive sampling. In this paper we follow this latter approach. In part, this choice is enforced by the presence of many theoretical results for flow and transport in heterogeneous porous media based on this statistical description. We also consider that, in light of the Borden and Cape Cod field-scale tracer tests, use of this parsimonious statistical description is not unwarranted; these natural-gradient tracer tests strongly suggest that, in these cases, this simple statistical description for the medium hydraulic conductivity does capture most of the significant features of flow and transport. However, these sites were also unusual in that the media, overall, are rather homogeneous; other sites where heterogeneity is a more dominate aspect of the medium could easily require a better representation of geologic features contained in the medium. It should be noted

that, even in these cases, a description based in probabibility may be feasible [e.g., *Carle and Fogg*, 1996] but would require a large parameter base.

In this paper, we discuss technical problems associated with MC simulation of three-dimensional flow and transport in heterogeneous porous media; the report also contains a summary of the velocity results from both fluid flow and plume modelling. The companion paper [*Naff et al.*, this issue] contains the results of examining second and higher moments of plumes generated by these MC simulations (i.e., macrodispersion, plume skewness and kurtosis). As multiple realizations of each scenario are generated, and as these realizations are essentially independent, we will be able to make statements concerning the quality of the results as well. In this paper, for example, the mean effective hydraulic conductivity and the standard deviation in effective hydraulic conductivity are given; this standard deviation will allow one to evaluate the likelihood that any one realization of the hydraulic conductivity field can be adequately modelled by the effective parameter. The scenarios discussed in this paper as affecting the plume or fluid velocity are the variance in the logarithm of the hydraulic conductivity, length scales and source size.

Monte-Carlo Scheme

The simulation domain consists of a parallelepipedic flow cell elongated in the mean flow direction [see *Burr et al.*, 1994, figure 1]; mean flow is either parallel or perpendicular to all domain faces (mean flow direction: x; transverse horizontal direction: y; transverse vertical direction: z). The domain is discretized into six-sided brick-shaped elements with a node at each corner; all elements have the same dimensions Δ_x, Δ_y and Δ_z. Flow is steady and fixed by constant head boundaries at opposite ends of the elongated cell; a random velocity field is created by forcing the flow to pass through a random hydraulic conductivity field. At time zero a conservative tracer source is introduced into the domain near the upgradient end of the cell; the upstream face of the cell is a Dirichlet boundary over which the concentrations are set to zero. With regard to both flow and transport, lateral boundaries are specified as no-flux boundaries; the downstream face is also a zero dispersive flux boundary. The tracer is allowed to drift with the random flow field; moments, calculated from the resulting simulated plume, are used to estimate the cloud velocity and dispersion. The MC simulator was constructed by placing critical subprograms to carry out these simulations in a Monte-Carlo loop; each iteration of the loop results in a new realization of the hydraulic conductivity field and a new solution to the flow and transport equations. The basic subprograms of the MC simulator are described in *Burr et al.* [1994]; these subprograms consist of a random field generator and flow and transport solvers which will be described here briefly. New realizations of the velocity and concentration fields, for each realization of the hydraulic conductivity field, are obtained by resolving the flow and transport problems for the same boundary and initial conditions. An efficient ORTHOMIN iterative solver [*Sudicky and McLaren*, 1992] was used to solve both the flow and Laplace-space transport matrix equations.

The spectral technique of *Robin et al.* [1993] is used to generate realizations of three-dimensional scalar hydraulic conductivity fields. The generated three-dimensional field ($m_x \times m_y \times m_z$) of discrete conductivity values is considerably larger than the simulation domain. The dimensions n_x, n_y and n_z of the simulation domain, in terms of element lengths Δ_x, Δ_y and Δ_z (the overall domain dimensions being $\Delta_x n_x$, $\Delta_y n_y$ and $\Delta_z n_z$), are one-half to two-thirds of the number of values as in the equivalent direction in the generated field: $m_x > n_x$, $m_y > n_y$ and $m_z > n_z$. The generator produces correlated normal random variates; the hydraulic conductivity field $K(\vec{x})$, $\vec{x} = (x, y, z)$, is assumed to be lognormally distributed such that $f(\vec{x}) = \ell n(K(\vec{x}))$ is a normal variate. Thus realizations of the $f(\vec{x})$ are actually produced by the spectral generator; the $K(\vec{x})$ field is obtained by exponentiation of $f(\vec{x})$ for each element within the simulation domain. Besides the field dimensions, input parameters required to generate a three-dimensional field consist of four target statistics: three length scales (λ_x, λ_y, and λ_z) corresponding to the principal axes of the parallelepiped and the variance of the logarithm of the hydraulic conductivity (σ_f^2). These statistics correspond to the parameters of the negative exponential autocovariance function used in the random-field generation process:

$$C_f(\vec{x} - \vec{x}') = \sigma_f^2 \exp\left[- \left(\frac{(x - x')^2}{\lambda_x^2} + \frac{(y - y')^2}{\lambda_y^2} + \frac{(z - z')^2}{\lambda_z^2} \right)^{1/2} \right] \tag{1}$$

where $x - x'$, $y - y'$ and $z - z'$ represent lag space in the x, y and z directions. When discretizing the simulation domain the element size was chosen such that at least two elements for every input length scale existed in each direction. The input horizontal length scales λ_x and λ_y were always chosen equal for these simulations. While the equivalent statistics for the generated fields are similar to the target statistics, there are invariably some deviations; thus it is imperative to estimate the actual output statistics from each field generated; with regard to the length scales λ_x, λ_y, and λ_z this proved to be an exceptionally difficult task as will be discussed subsequently.

The flow simulator is based on a finite element scheme wherein values for heads, based on the imposed boundary conditions, are obtained at each node. The computational method employs the influence coefficient technique whereby the six closest adjacent nodes aligned along the principal directions influence a given node, rather than all the 26 surrounding nodes in the adjacent elements. Components of the fluid specific discharges, for each element within the domain, are obtained from head information at the eight elemental nodes and the generated scalar hydraulic conductivity for that element; the elemental velocity components V_x, V_y and V_z are obtained from the elemental specific discharge components by dividing by the elemental porosity (assumed constant in this study). Boundary conditions imposed on the flow field cause the resulting elemental velocity field to be nonstationary; this non-stationarity is most prevalent near the lateral boundaries. To partially offset this deviation from nonstationary conditions a rind of elements, on or near the domain boundary and lateral to the mean flow direction, is set aside from which no velocity information is taken, and for which a simulation is terminated if a nodal concentration within the rind is excessive at a given time step. This exclusion zone will be described in more detail in a subsequent section.

For these simulations, the Laplace-transform finite-element technique was again used to solve the transport equation; this numerical method has the advantage that, for relatively coarse grides, solutions to the transport equation exhibit essentially no numerical dispersion [*Sudicky*, 1989]. Dispersion at the local scale is governed by longitudinal (α_ℓ) and transverse (α_t) dispersivities which are assumed to be constant; as the velocity field is random, the local dispersion coefficients themselves are also random. The transport equation in Laplace transform space, for a nonreactive tracer, can be written

$$p\hat{c} + \vec{V} \cdot \nabla \hat{c} - \nabla \cdot \mathbf{d} \nabla \hat{c} \;=\; c(\vec{x}, 0) \tag{2}$$

where p is the Laplace variable: $\mathcal{L}[c(t,\vec{x});t \rightarrow p] = \hat{c}(p,\vec{x})$. The second-order tensor of dispersion coefficients $\mathbf{d}$ can be expressed as

$$\mathbf{d} = \begin{bmatrix} d_{xx} & d_{xy} & d_{xz} \\ d_{yx} & d_{yy} & d_{yz} \\ d_{zx} & d_{zy} & d_{zz} \end{bmatrix} = \alpha_t V \mathbf{I} + (\alpha_\ell - \alpha_t)\frac{\vec{V}\vec{V}^T}{V}$$

where $\mathbf{I}$ is a 3×3 identity matrix, $V = \sqrt{\vec{V} \cdot \vec{V}}$ and $\vec{V} = (V_x, V_y, V_z)$. The right-hand side of equation (2) represents the initial condition for the transport problem. When this equation is discretized using a Galerkin finite-element method, this initial condition becomes a set of nodes at which the concentration is initially non-zero; for the purposes of the MC simulation these nodes form a small box near the upstream end of the flow cell in which the concentration is initially set to unity. The initial box is usually two vertical length scales λ_z thick and at least two elements wide and deep. This source box must also be relatively distant from the x and y boundaries of the flow cell if the resulting plume simulation is not to be impacted by these boundaries; this consideration generally limited the size of the source region. As the simulation proceeds, these initial concentrations are advected by the random velocity field and dispersed by the local dispersion coefficients. It should be noted that, for purposes of computational efficiency, the influence coefficient technique was again used when approximating the local dispersive flux. Thus, only the nearest six nodes from the surrounding brick-shaped elements are used in the local dispersive flux approximation in the Galerkin finite-element scheme; the result is that only those cross-derivative terms which corresponding to this template are retained in the global matrix assembly. While this minimal retention of cross-derivative information in the numerical approximation introduces a certain amount of error, our experience indicates that it is a relatively modest source of error in the overall MC scheme. The Laplace-space solution was inverted using the scheme developed by *de Hoog et al.* [1982]; spatial moments were calculated for every

plume realization, and the concentration field for each node was added to previous realizations so that individual realization plume statistics could be compared to ensemble mean plume statistics.

In the initial stages of this project, considerable time was spent determining the appropriate mesh size for the simulation domain. In this case, not only does one have to be concerned about the transport of a sharp front, but also by the sharp contrast in the dispersion coefficients from element to element. As our interest was centered around large-time plume moments, concentration fields were obtained only after the plume had traveled at least one length scale λ_x; indeed the Laplace inversion scheme was set up to return concentration fields beginning with a travel time corresponding to a mean plume travel distance of at least one length scale λ_x. The use of a minimum travel time corresponding to at least one length scale λ_x allowed us to bypass numerically difficult computations associated with resolving a sharp front; resolution of the early-time sharp front is a computational necessity associated with most time-stepping algorithms. We found, by experimentation, that our simulations could be accommodated by a relatively coarse grid Peclet number (Δ_x/α_ℓ) of 3.33; this value worked well over the range of σ_f^2 values used in this study (0.09 to 0.9). As the variance in $f(\vec{x})$ and therefore $K(\vec{x})$ increased so did the contrast in the V_x component of the velocity field from element to element; this contrast resulted in a commensurate contrast in the transverse dispersion coefficients d_{yy} and d_{zz} which necessitated refinement of the mesh in the lateral directions. Experimentation with a deterministic heterogeneity embedded in an otherwise uniform medium indicated that, when a contrast existed in which the hydraulic conductivity of the deterministic heterogeneity was ten times that of the rest of the medium, large oscillations in the concentration field resulted unless the ratio Δ_y/α_t or Δ_z/α_t was about 25 or less than. Since α_t was generally taken to be one centimeter in this study, this restriction forced the mesh spacing to generally be 0.25 meters or less. To accommodate this mesh spacing without generating an even larger hydraulic

conductivity field, a method of further subdividing the existing domain, with a hydraulic conductivity field generated for a coarser mesh, was devised.

The computed concentration field was monitored for oscillation from realization to realization by observing two quantities: the ratio of $c_{min}(t)$ to $c_{max}(t)$ and the ratio of the number of negative concentration nodes to positive concentration nodes (nodal concentrations less than $c_{max}(t) \times 10^{-4}$ were considered to be zero). If the ratio $c_{min}(t)$ to $c_{max}(t)$ and the ratio of negative to positive nodes were both greater that 0.01, or if either ratio alone was greater than 0.1, then it was considered likely that the computed concentration field contained significant oscillation and therefore was deemed unacceptable. If either criteria alone exceeded the 0.01 threshold, but was less than 0.1, then the likelihood of significant oscillation was considered to be small to moderate. In most cases, neither criterion exceeded the 0.01 threshold. However, when the plume had traveled only one or two length scales λ_x, it was not uncommon to see that the 0.01 threshold for the $c_{min}(t)$ to $c_{max}(t)$ criterion to be approached and occasionally exceeded. Also, in late time it was not uncommon to see a growth in the ratio of negative to positive nodes such that the 0.01 threshold was approached. In our experience, moment calculations were found to be degraded by oscillation primarily when both the number of negative nodes was excessive and the maximum negative value of the concentration solution was uncommonly large.

In general, our goal was to see the plume migrate over approximately ten or more length scales λ_x; from previous work [*Burr et al.*, 1994], it appeared that travel distances of this order would be sufficient to define asymptotic macrodispersivities. To accomplish this goal it was necessary to construct a domain with enough lateral width and depth to accommodate all transverse dispersion plus lateral deviation of the plume from its mean flow path and long enough to accommodate all longitudinal variation in the mean plume

velocity as well as all longitudinal dispersion. To ameliorate the effect of the longitudinal velocity variation on the overall domain dimension $\Delta_x n_x$, a procedure for conditioning the hydraulic conductivity of the initial box to a certain range of values was adopted; this procedure will be described in a subsequent section. Given the above restrictions on mesh size, our domains generally contained on the order of 800,000 to 900,000 elements and, given the space requirements of the ORTHOMIN solver, could require on the order of one Gbyte of memory.

Because these MC simulations depend upon numerical models to approximate flow and transport of the tracer cloud, the amount of numerical error introduced by these models can always be questioned. Previous work with these numerical techniques suggest that, for a homogeneous medium and at the discretization levels used herein, this source of error would be very small [*Sudicky*, 1989; *Sudicky and McLaren*, 1992]. For instance, if one examines examines plot of the macrodispersivities versus variance in log hydraulic conductivity presented in the companion paper [*Naff et al.*, this issue, Figure 3], it is apparent that, as the variance in log hydraulic conductivity approaches zero, the estimated dispersivities approach the input, local dispersivities. However, the current simulations incorporate a heterogeneous medium and the numerical error associated with such simulations is less well understood. Previous work by *Burr* [1992] suggests that reasonable agreement exists between velocity covariances estimated from data obtained from flow models similar to those used herein and analytical, first-order approximations of the velocity covariances. On the other hand, very recent work by *Cai et al.* [1997], indicate that, for heterogeneity which produces very large contrasts in the hydraulic conductivity from cell to cell, the correct velocity field may not always be captured by the current numerical technique unless the computational grid is rather fine. While this problem cannot be ruled out in the current simulations, we rather believe that the smoother hydraulic conductivity field associated with the random field generator used in this study make this source of error less

significant. The larger problem, as far as these simulations are concerned, is the existence of small oscillations in the concentration field from the solution of the transport equation. As discussed previously, we attempted to control this source of error by refining the grid mesh as needed. Except possibly for the very largest variances in hydraulic conditivity used in this study, it is unlikely that numerical error from the modelling technique significantly impacts the moment results reported herein; rather, as discussed subsequently, a more likely problem is the limited number of realizations used in these MC simulations.

Estimation of Length Scales

As noted previously, the spectral technique for generating random fields does not recapture the input or target parameters used to initiate the generation process; this results because the spectral random field generator is a discrete approximation of a continuous process [*Robin et al.*, 1993]. A certain amount of information is lost when the continuous process is discretized and when the infinite domain of its definition is approximated by a finite domain. The reason for discretizing is basically efficiency: the fast-Fourier transform (FFT) can be used to invert the discretized process so as to obtain a complete field of correlated normal random variates with one application of the FFT. With regard to the actual variance of the process, the discretization approximation is not a serious inconvenience: the resulting field can be resampled and the variance estimated. Indeed, as multiple realizations of the process exist, the ensemble mean and ensemble variance of the variance statistic for individual realizations can be determined. However no equivalent statistics exist for the length scales λ_x, λ_y and λ_z, leaving one with the problem of obtaining an independent estimate of these parameters.

A common technique of estimating the length scales is to first estimate the autocovariance function (or variogram) and then to fit a model equation for the autocovariance function (ACF) to this information [see e.g., *Burr et al.*, 1994]. For this study the model equation for the ACF would be (1); the length scales λ_x, λ_y and λ_z become the fitting parameters. A commonly used estimator for the ACF, in one dimension and as applied to a single realization, is

$$\hat{C}_j = \frac{1}{n-j}\sum_{i=1}^{n-j}(f_i - \bar{f})(f_{i+j} - \bar{f}) \tag{3}$$

where $\hat{C}_j$ is the sample ACF, j is the lag number, n is the sample size and

$$\bar{f} = \frac{1}{n}\sum_{i=1}^{n} f_i$$

is the sample mean of the process f_i. This sample ACF is known to have the property that

$$\sum_{j=-(n-1)}^{n-1} \left(1 - \left|\frac{j}{n}\right|\right) \hat{C}_j = 0 \tag{4}$$

(This result is a variant of equation (2.1) given by *Percival* [1993].) Note that $\hat{C}_0$ (the sample variance) and the weights $1 - |j/n|$ must be positive. If the lag region near the origin is positive then, in order to accommodate (4), the sample ACF at some distance from the origin must be largely negative. Also, as the weights $1 - |j/n|$ tend to zero for large lags j, this negative region cannot be too distant from the origin. As with most ACF estimators, (3) is biased; behavior (4) of (3) probably results from the particular nature of this bias. The autocovariance estimator (3) is pathological in that its sample ACF may be expected to go negative, even though the actual autocorrelation function of the process may be entirely non-negative. This behavior of the ACF estimator (3) is particularly vexing if one is intent on estimating the length scales λ_x, λ_y and λ_z from sample ACF data by some sort of residual minimization scheme; unwarranted negative estimates for the ACF in the tail region falsely weight the results toward smaller length-scale estimates. In three dimensions a large fringe of negative autocovariance estimates can heavily influence regression results. Other ACF estimation schemes we considered suffered similar debilities as (3), although often not as extreme.

A potential solution to the problem of length-scale estimation would be to use the least-biased ACF estimator available in conjunction with a parameter estimation scheme which strongly weights the small lag information [*Cressie*, 1991]. However, we considered that this procedure would be little or no better than the scheme that we eventually did use to estimate length scales. The procedure we employed uses the integral scale which, for the x direction, is defined from the three-dimensional ACF $C_f(\vec{s})$ as

$$\lambda_x \;=\; \frac{1}{\sigma_f^2} \int_0^{+\infty} C_f(\vec{s})\big|_{s_y=0, s_z=0}\, ds_x \;=\; \frac{1}{2\sigma_f^2} \int_{-\infty}^{+\infty} C_f(\vec{s})\big|_{s_y=0, s_z=0}\, ds_x \tag{5}$$

where $\vec{s} = \vec{x} - \vec{x}'$. Because the ACF is related to its spectrum $S_f(\vec{\omega})$ by the Fourier transform, where $\vec{\omega} = (\omega_x, \omega_y, \omega_z)$ is a vector of the Fourier wave numbers, such that

$$C_f(\vec{s}) \;=\; \int_{-\infty}^{+\infty} \int_{-\infty}^{+\infty} \int_{-\infty}^{+\infty} exp[i\vec{s} \cdot \vec{\omega}] S_f(\vec{\omega})\; d\vec{\omega} \tag{6}$$

the integral scale λ_x can be obtained from the spectrum:

$$\lambda_x \;=\; \frac{\pi}{\sigma_f^2} \left[\int_{-\infty}^{+\infty} \int_{-\infty}^{+\infty} S_f(\vec{\omega})\; d\omega_y d\omega_z \right] \Bigg|_{\omega_x = 0} \tag{7}$$

which results from applying (5) to (6). Since the field generator used in this study utilizes the spectrum of (1) discretized over a finite domain, this discretized spectrum can be summed directly to form an approximation of (7) [*Robin et al.*, 1993]; this procedure yields estimates of the length scales $\hat{\lambda}_x$, $\hat{\lambda}_y$ and $\hat{\lambda}_z$ that are not perturbed by the random number generator. That is, only effects of discretizing $f(\vec{x})$ in a finite domain is accounted for by this direct spectral procedure; any effect resulting from the multiplicative zero-mean random noise added in the field generation is implicitly ignored. In essence, an approximation of a length scale obtained by this scheme should be approximately equivalent to the mean of an estimate in which this randomness is accounted for.

Figure 1 shows the mean sample ACF for lags in the x direction as estimated from 20 realizations of the process; the sample ACF was obtained using a three-dimensional estimator similar to (3) but slightly less biased. The sample ACFs on which the mean was constructed were estimated from generated three-dimensional fields $f(\vec{x})$ in which an input length scale λ_x for the generation process was six meters (λ_y was four meters and λ_z was two meters). Each generated realization had dimensions of 40 m, 20 m and 10 m in the x, y and z directions; the maximum allowed lag distance for purposes of correlation estimation was 18 m, 12 m and 6 m in each of these directions. The error bars in Figure 1 represent the approximate standard error of the mean ACF; the standard deviation for the sample ACF was estimated from the 20 sample ACFs obtained from the individual realizations.

Using the estimation procedure based on the descritized spectrum, $\hat{\lambda}_x$ was estimated to be 6.16 meters ($\hat{\lambda}_y = 4.21\ m$ and $\hat{\lambda}_z = 1.96\ m$); using (1), this result is represented as a dashed line on Figure 1. A weighted least squares procedure, using the standard error estimates of the mean sample ACF as weights, was also used to estimate length scales directly from the three-dimensional mean sample ACF data; these results are present as a solid line in Figure 1 ($\hat{\lambda}_x = 5.46\ m$, $\hat{\lambda}_y = 3.06\ m$ and $\hat{\lambda}_z = 1.54\ m$). The fit is clearly inferior; we suspect that the length scales are underestimated because of the presences of negative values for the mean sample ACF for large lags in combinations of the x, y and z directions (the mean sample ACF for large lags in the individual x, y or z directions demonstrated no negative values). For actual field data, it is probable that either a better weighting technique or even a data censoring scheme could be devised to help remedy this problem; for this study, we considered that the estimation scheme based on the discretized spectrum to be at least comparable in quality to any scheme based on least squares estimation and the sample ACF data.

Boundary Effects

The presence of boundary effects on the flow field in heterogeneous porous media has been recognized for some time [e.g., *Naff and Vecchia*, 1986, *Bellin et al.*, 1992]. The objective of most MC simulations of subsurface transport is to emulate an infinite domain; thus efforts are made to keep the transport aspect of the simulation as free of the influence these conditions as possible. We examined the velocity field for the effects of boundary conditions; in particular, the variances in V_x, V_y and V_z velocity components were estimated along the midlines of the domain. That is, along rows of elements forming the midlines of the domain in the x, y and z directions the velocity components V_x, V_y and V_z were collected from every realization of the MC experiment; these data, over multiple realizations, were used to calculate the sample variances of the three velocity components for each element. The estimated variances for each element were based on 900 realizations of the flow process, obtained by running the MC simulator in a flow-only mode. For these simulations, the input horizontal length scales λ_x and λ_y were chosen equal. The simulations were made with two different variances in the hydraulic conductivity field ($\hat{\sigma}_f^2 \approx 0.09$ and $\hat{\sigma}_f^2 \approx 0.9$) and two different anisotropy ratios ($\hat{\lambda}_h/\hat{\lambda}_z = 3.9$ and $\hat{\lambda}_h/\hat{\lambda}_z = 21$). Here, because of discretization factors discussed previously, the output length scales $\hat{\lambda}_x$ and $\hat{\lambda}_y$ are not exactly equal; a common horizontal length scale is approximated as $\hat{\lambda}_h = \sqrt{\hat{\lambda}_x \hat{\lambda}_y}$ (the difference in $\hat{\lambda}_x$ and $\hat{\lambda}_y$ are small: $\hat{\lambda}_x = 5.79\ m$ and $\hat{\lambda}_y = 5.63\ m$ in one case and $\hat{\lambda}_x = 1.23\ m$ and $\hat{\lambda}_y = 1.22\ m$ in the other.).

The effect of the no-flow boundaries on the V_y and V_z components are shown in Figures 2, 3 and 4; all variances have been normalized by the mean of the V_x velocity component. Note that, even with 900 realizations, the depicted relative variances are yet rather noisy; however, a number of trends are detectable. The variance in V_y in the y direction and V_z in the z direction tend to zero as the lateral domain boundary is approached. In the case

of the variance of V_y in the y direction (Figure 2), at a distance somewhat greater than one length scale $\hat{\lambda}_y$ from the boundary, the velocity variance profiles approach a somewhat constant value over the center of the flow cell. The medium hydraulic conductivity is essentially isotropic in the x-y plane, and varies more slowly in this plane than in the z direction. For the variance of V_z in the z direction (Figure 3), a constant variance value is approached only after a distance of two to three length scales $\hat{\lambda}_z$ from the flow-cell boundary. The z direction is the direction of more rapid variation in the scalar $f(\vec{x})$ field; this result suggests that the effect of anisotropy on the velocity variance is to cause the velocity component coincidental with the direction of the most rapid variation in $f(\vec{x})$ to have the largest boundary transition zone. Note that the variance in V_y in the z direction (Figure 3) and V_z in the y direction (Figure 2) are only mildly affected by the presence of no-flow boundaries, exhibiting a tendency to increase slightly near a boundary.

The variance of V_x in the x, y and z directions demonstrated no visible effect due to the imposition of boundary conditions; variance values of the V_x component from elements next to a no-flow or constant head boundary were essentially indistinguishable from the rest of the variance profile. However, the constant head boundary conditions do exert considerable influence on the variance in the V_y and V_z velocity components, as demonstrated by Figure 4. In contrast to the lateral directions, the V_z component generally exhibits a rather abrupt transition from essential zero variance near the constant head boundaries to nearly constant variance values over the interior of the domain. For the V_y component, a transition zone of at least one length scale $\hat{\lambda}_x$ may be necessary before a somewhat constant variance in the x direction is obtained. This broader transition zone for the V_y component is associated with the smaller value of the variance in log hydraulic conductivity ($\hat{\sigma}_f^2 \approx 0.09$); when $\hat{\sigma}_f^2 \approx 0.9$ then the width of the transition zone is not unlike that of the V_z component. Why the transition zone for V_y in the x direction should be broader for the smaller value of $\hat{\sigma}_f^2$ than for the larger $\hat{\sigma}_f^2$ value is not understood.

As mentioned earlier, a boundary exclusion zone interior to the flow cell, from which no flow or transport data would be collected, was created to ameliorate for these nonstationary flow field characteristics. The zone consisted of a rind of elements parallel to the domain boundaries from which no data, whether velocity or concentration, was collected. The interior of the exclusion zone defined a detection boundary along which plume concentrations were monitored; in the absence of an exclusion zone, the flow cell boundary itself became the detection boundary. Plume moment information was excluded from the data sets by simply terminating a simulation if the nodal concentration on the detection boundary exceeded three percent of the maximum concentration. The size of these exclusion zones had to be balanced by the memory requirements resulting from the rather fine discretization used in the modelling effort; this trade-off resulted in the use of only a small exclusion zones lateral to the mean flow direction and no exclusion zone in the x direction (the domain limits served as the detection boundary). The lateral boundary exclusion zone consisted of a region one input length scale λ_y or λ_z thick adjoining the y and z boundaries. As most of the simulations were run with an input anisotropy λ_x/λ_z of 10, it is clear that some deviation from a free domain, particularly in the z direction was unavoidable. For the velocity field, most of the statistics collected concern the V_x velocity component and therefore are not as likely to be influenced by boundary effects. Plume moments, to be discussed largely in the companion paper, are more likely to have been affected. As plume simulation was discontinued when the detection zone was encountered, the first instance of mass arrival at the downstream boundary was sufficient to cause termination. That the leading edge of the plume would encounter little or no variation in the V_y and V_z velocity components near the downstream boundary was considered to be of little or no consequence to the overall moment calculations for the plume. On the other hand, the persistence of the boundary effects in the z direction is more likely to have affected, to a small degree, the vertical transverse second moment. Overall, considering the

quality of the estimated plume moments as determined from a typical 20 realization MC experiment, it is usually not feasible to separate small effects resulting from the imposition of boundary conditions from simple noise in the simulation.

Effect of Source Region Hydraulic Conductivity on First Moment

The average hydraulic conductivity of the source region from whence the plume emanates can affect immensely the overall travel time of the plume. To illustrate this effect, 200 realizations of the hydraulic conductivity field for a given flow cell geometry were generated. The x, y and z dimensions of the flow cell were 60 m, 14 m and 8.5 m; a source box with dimensions $0.66 \times 0.5 \times 0.25$ m^3, centered in the flow cell two meters from the upstream boundary, was given an initial concentration of unity. Input length scales of $\lambda_x = \lambda_y = 2.5$ meters and $\lambda_z = 0.25$ meters were used in the simulations; the variance in $\ell n\, K(\vec{x})$ was estimated to be 0.44. The spatial-average hydraulic conductivity of the source region for each of the 200 realizations was calculated. A histogram of these mean hydraulic conductivities of the source region was constructed and estimates of the mean and standard deviation, $\hat{\mu}_m$ and $\hat{\sigma}_m$, were obtained. The histogram was divided into six intervals based on the estimated standard deviation of the source region mean hydraulic conductivity: $-\infty$ to $-2\hat{\sigma}_m + \hat{\mu}_m$, $-2\hat{\sigma}_m + \hat{\mu}_m$ to $-\hat{\sigma}_m + \hat{\mu}_m$, $-\hat{\sigma}_m + \hat{\mu}_m$ to $\hat{\mu}_m$, $\hat{\mu}_m$ to $\hat{\sigma}_m + \hat{\mu}_m$, $\hat{\sigma}_m + \hat{\mu}_m$ to $2\hat{\sigma}_m + \hat{\mu}_m$, and $2\hat{\sigma}_m + \hat{\mu}_m$ to ∞. From each of these six intervals, five realizations were selected for transport modelling. Mean moment results for every interval, obtained from the five plume simulations, give approximate information as to the effect of source-region hydraulic conductivity on plume behavior. The mean first moment results, describing the approximate mean plume location $\langle X_c \rangle$ in the x direction for each of this six intervals, is depicted in Figure 5. Although the slope of these first moments tends to become constant and similar with increasing travel time, the effect of variation in the source region hydraulic conductivity is to cause considerable deviation in the mean arrival time of the plume at a downgradient point; a maximum difference of almost three length scales in travel distance of $\langle X_c \rangle$ is to be observed from this figure.

For the modeller, the fact that variation in hydraulic conductivity of the source region can cause the plume to have this amount of initial variation in mean velocity has consequences as to the domain size. To incorporate the initial velocity variation demonstrated in Figure 5 would involve making the domain sufficiently large to accommodate the approximate three length scales of travel variation in $\langle X_c \rangle$; an enlargement of the domain to accommodate this variation would be the minimum possible as neither the amount of variation in each X_c profile nor the effect of increased capacity for lateral dispersion on the overall domain width have been taken into account. This results because our strategy was to use a single time interval, over all realizations, to define the late-time macrodispersion coefficient [see *Naff et al.*, this issue]. As late-time plume behavior is the principle objective of this study, this initial variation in the plume location was considered to be more of a nuisance factor than an important aspect of the study. Thus, for reasons of computational efficiency and interpretation of results, an alternate to a completely unconditioned simulation was sought.

One can obtain the composite mean plume centroid $\langle\langle X_c \rangle\rangle$ by weighting the individual mean centroids $\langle X_c \rangle$ by the relative number of realizations in each histogram interval; the composite centroid is shown as a solid line on Figure 5. The $\langle X_c \rangle$ profile for the histogram interval $-\hat{\sigma}_m + \hat{\mu}_m$ to $\hat{\mu}_m$ corresponds reasonably well to this composite. Primarily as a memory saving feature, all simulations in this study were selected from those realizations between one negative standard deviation of the mean and the mean of the mean source-region hydraulic conductivity. Accomplishment of this objective entailed running, for every MC scenario, a pre-Monte-Carlo run in which 200 realizations of the flow-cell hydraulic conductivity were generated; from these 200 realizations, 40 or more would have a mean source region hydraulic conductivity in the interval $-\hat{\sigma}_m + \hat{\mu}_m$ to $\hat{\mu}_m$; from these 40 or more realizations, a subset was selected to test the scenario in question. In essence,

the tracer results presented in this paper are conditioned by using this operation to preselect the source-region hydraulic conductivities. While no appreciable effect of this form of conditioning was noted on first-moment results from these simulations, some effect on the second-central moments may be present; this possibility is noted in the conclusions of the companion paper [*Naff et al.*, this issue].

One result of this form of conditioning is that the variance in plume centroid location X_c could be significantly diminished as compared to MC simulations where the source region hydraulic conductivity is unrestrained. To examine this possibility, the initial five realizations in the $-\hat{\sigma}_m + \hat{\mu}_m$ to $\hat{\mu}_m$ histogram interval were extended to a typical 20 realization set; then the plume centroid variance, $\hat{\sigma}_{X_c}$, from this conditioned MC simulation was compared to the centroid variance obtained from the composite set. The results of this comparison indicated that any difference in the two variances is not sufficient to be detectable with the error involved in a typical 20 realization MC simulation. In this case, the conditioned simulation actually yielded more variance in X_c than did the composite simulation results, although the late-time slopes of the two variance curves were nearly identical. This latter result is probably an indicator of one of the conclusions of this study: it is difficult to make comparisons between moment results from these MC simulations, unless the difference being sought is large on its own accord or an immense number of realizations are utilized in the simulations.

Effective Hydraulic Conductivity

In the process of performing MC simulations, an immense amount of data is collected which is not directly related to the plume migration; this data often can be used to analyze ancillary phenomena. One of these phenomena is the effective hydraulic conductivity of the flow cell; the effective hydraulic conductivity for the x direction is defined as

$$K_{eff} = \frac{E[q_x]}{-E[\partial h/\partial x]}$$

where $E[\partial h/\partial x]$ is the mean gradient of the flow cell and $E[q_x]$ is the mean specific discharge in the x direction. Estimates of mean heads $\langle h(x)\rangle$ at each location x are obtained by first averaging, for each realization, over the interior heads within y,z cross sections and then by averaging those single-realization means over the realizations in the MC simulation. The mean gradient was estimated by fitting a straight line to the mean heads, exclusive of a very few locations in the immediate vicinity of the x boundaries; a straight line provided a very good fit to the x-direction mean head data. As both mean and gradient estimators are linear, $\langle \partial h/\partial x\rangle = \partial\langle h\rangle/\partial x$. Specific discharge information is routinely collected for the interior elements (all flow cell elements less the boundary exclusion elements); when averaged over the interior elements and over realizations, an approximation $\langle q_x\rangle$ for the mean specific discharge in the x-direction is formed. Given that $E[q_x] \approx \langle q_x\rangle$ and $E[\partial h/\partial x] \approx \langle \partial h/\partial x\rangle$ are reasonable approximations, then the effective hydraulic conductivity can be estimated from the above form. Two scenarios, one for different variances in log hydraulic conductivity and another for different anisotropy ratios, are reported on herein.

For the scenario with different variances in the hydraulic conductivity, a flow cell with dimensions $60 \times 15 \times 10\ m^3$ (x,y,z) with a head difference of 0.2 meters across the cell was used. The geometric mean hydraulic conductivity K_ℓ, as calculated over all 20 realizations in these simulations, was $9.97\ m/d$. The anisotropy, as calculated from $\hat{\lambda}_h/\hat{\lambda}_z$, where $\hat{\lambda}_h = \sqrt{\hat{\lambda}_x \hat{\lambda}_y}$, was 10.0. The mean gradient, because of the imposed constant-head boundary conditions, is very nearly constant from simulation to simulation. The resulting effective hydraulic conductivity K_{eff}, for varying values of $\hat{\sigma}_f^2$, is presented in Figure 6. Assuming that the variance of the mean gradient estimate $\langle \partial h/\partial x \rangle$ is small and therefore negligible, error bars for the K_{eff} can be obtained from the standard error for the estimated mean of q_x, as determined from the realization to realization variation in q_x; these error bars, as might be expected, increase with increasing variance in the log hydraulic conductivity. The error bars indicate that K_{eff} for the smaller $\hat{\sigma}_f^2$ are quite well determined, but less so as $\hat{\sigma}_f^2$ approaches unity.

A theoretical first-order relation for the effective hydraulic conductivity, given by *Gelhar and Axness* [1983, equation (59)], is

$$K_x \approx K_\ell + K_\ell \left(\frac{1}{2} - g_{11} \right) \sigma_f^2 \tag{8}$$

where K_x is the x direction component of the effective hydraulic conductivity tensor, and g_{11} is the following correction factor for the statistical anisotropy ρ of the medium:

$$g_{11} = \frac{1}{2\left(\rho^2 - 1\right)} \left[\frac{\rho^2}{\sqrt{\rho^2 - 1}} \arctan\left(\sqrt{\rho^2 - 1} \right) - 1 \right] \tag{9}$$

[*Gelhar and Axness*, 1983, equation 53]. We will consider that, for the purposes of this study, $\rho = \hat{\lambda}_h/\hat{\lambda}_z$. The function $g_{11}(\rho)$ is monotonically decreasing such that, as $\rho \rightarrow \infty$, $g_{11} \rightarrow 0$; thus $K_\ell(1 + \sigma_f^2/2)$ is the first-order approximation of K_x for this asymptote. For this case, an exact expression for the effective hydraulic conductivity is available: $K_x \rightarrow K_\ell \; exp\left(\sigma_f^2/2\right)$ as $\rho \rightarrow \infty$; for $\sigma_f^2 > 0$, this expression is always greater than the first-order approximation [*Indelman and Abramovich*, 1994]. Equation (8), evaluated using the ratio $\rho = 10.0$ as the appropriate measure of medium statistical anisotropy, is depicted as a continuous function of σ_f^2 in Figure 6 (dashed line). For small $\hat{\sigma}_f^2$ the fit of the theoretical to experimental results appears quite good; only as $\hat{\sigma}_f^2$ approaches unity does the fit deviate significantly. A fit of a quadratic polynomial to the experimental K_{eff} data of Figure 6 indicates that the relation of K_{eff} to $\hat{\sigma}_f^2$ is

$$K_{eff} \;=\; 10.00 + 4.11\hat{\sigma}_f^2 + 0.53\hat{\sigma}_f^4 \tag{10}$$

Given that (10) is representative of a higher-order approximation, a first-order approximation, equivalent to (8), can be obtained by truncating this expression after the $\hat{\sigma}_f^2$ term:

$$K_{eff} \;\approx\; 10.00 + 4.11\hat{\sigma}_f^2$$

Using a statistical anisotropy of $\rho = 10.0$ in (9), a value of 0.0696 is obtained for g_{11}; the quantity $K_\ell\,(\frac{1}{2} - g_{11})$, given that $K_\ell = 9.97\ m/d$, is about $4.3\ m/d$. To obtain the $4.11\ m/d$ value suggested by equation (10), a value for g_{11} of about 0.09 is necessary; expression (9) will yield this value only if the statistical anisotropy is about eight; as noted subsequently, this slight difference is probably attributable to the insensitivity of K_x to the statistical anisotropy.

Gelhar and Axness, [1983, equation 60] also suggest that an infinite-order extension of (8) might be

$$K_x \;=\; K_\ell \; exp\left[\left(\frac{1}{2} - g_{11}\right)\sigma_f^2\right] \tag{11}$$

A second-order approximation, based on this conjecture, results if the exponential in (11) is expanded such that

$$K_x \approx K_\ell + K_\ell \left(\frac{1}{2} - g_{11}\right)\sigma_f^2 + \frac{K_\ell}{2}\left(\frac{1}{2} - g_{11}\right)^2 \sigma_f^4 \tag{12}$$

If one assumes that $K_\ell \left(\frac{1}{2} - g_{11}\right) = 4.11\ m/d$, and that $K_\ell = 10.0\ m/d$, then $K_\ell \left(\frac{1}{2} - g_{11}\right)^2 /2 = 0.84\ m/d$, which is significantly larger than the coefficient for the second-order term in (10). Thus, these Monte Carlo results don't appear to sustain the conjectured exponential relation. The second-order analysis by *Indelman and Abramovich* [1994, equation (25)] indicates that a correction factor must be added to the second-order term in (12) such that

$$K_x \approx K_\ell + K_\ell \left(\frac{1}{2} - g_{11}\right)\sigma_f^2 + \frac{K_\ell}{2}\left[\left(\frac{1}{2} - g_{11}\right)^2 + \gamma_{11}\right]\sigma_f^4 \tag{13}$$

where γ_{11} is a complex integral of the $f(\vec{x})$ autocorrelation function; their Figure 4 indicates that $-2\gamma_{11}$ is unlikely to exceed 0.45 and, for $\rho = 10.0$, is on the order of 0.3. The difference between the coefficients of the second-order terms in (10) and (13) suggests that $K_\ell\ \gamma_{11}/2 \approx -0.31$ and that $-2\gamma_{11} \approx 0.12$, or about half that one would expect from the second-order correction as derived by *Indelman and Abramovich* [1994]. The large coefficient for the quadratic term given in (10) indicates that the γ_{11} values depicted in Figure 4 of *Indelman and Abramovich* [1994] are excessive; however, without a correction of this nature, (12) alone produces even more quadratic curvature. It would seem that, for the second-order approximation, a correction factor of this nature is needed, but may not be as large as that indicated by *Indelman and Abramovich* [1994].

To test for the effect of anisotropy on flow, an initial flow cell $60 \times 14 \times 24\ m^3$ was constructed wherein the input length scales were $\lambda_x = \lambda_y = 3\ m$ and $\lambda_z = 0.6\ m$. Different anisotropies were effected by shrinking the flow cell in the z direction while maintaining the ratio of the original input length scale λ_z to the original z dimension of the flow cell (i.e., $\Delta_z n_z/\lambda_z$ was maintained at 40). Effectively, the input length scales λ_x and λ_y were maintained constant at three meters for all simulations while λ_z was allowed to vary. The estimated variance in the log hydraulic conductivity, $\hat{\sigma}_f^2$, was 0.443 and the geometric mean hydraulic conductivity was $K_\ell = 9.78\ m/d$; the head difference across the cell was again $0.2\ m$. The resulting effective hydraulic conductivity for these simulations, as a function of the estimate anisotropy ratio $\hat{\lambda}_h/\hat{\lambda}_z$, is depicted in Figure 7; the error bars were constructed as before. The first-order approximation (8), evaluated for the above parameter estimates, is plotted on this figure as a dashed line. The fit of theoretical to experimental, in this case, is rather good, suggesting that the function g_{11} of *Gelhar and Axness* [1983] adequately compensates for variation in the statistical anisotropy. It is noteworthy that the second-order analysis of *Indelman and Abramovich* [1994, their Figure 7] indicates that, for an anisotropic ratio somewhat less than ten, the first-order approximation should cross over the effective hydraulic conductivity curve, as occurs in our Figure 7. Because $exp(\sigma_f^2/2) \geq 1 + \sigma_f^2/2$, it is to be expected that K_{eff} will eventually exceed the first-order approximation as $\rho \to \infty$. However, the large error bars associated with the MC results suggest that the location of the cross-over point is difficult to predict with confidence; this similarity between the MC results and the second-order analysis of *Indelman and Abramovich* [1994] could be coincidental, although it seems unlikely. The theoretical, first-order curve tends to flatten as the statistical anisotropy increases; that is, the effective hydraulic conductivity becomes less sensitive to changes in this parameter. The theoretical maximum value that K_{eff} can achieve, under these circumstances, is the arithmetic

mean of the hydraulic conductivity, which in this case is $K_\ell \; exp(\sigma_f^2/2) \approx 12.2 \; m/d$; the maximum value achievable by the first-order approximation is $11.9 \; m/d$. While these asymptotes are approached only slowly with increasing statistical anisotropy, 90% of the change (from $10 \; m/d$ to $12 \; m/d$) would be obtained when an anisotropy ratio of 20 is reached.

A second-order approximation, based on equation (13), can be devised from (12) by first evaluating this expression with $\sigma_f^2 = 0.443$ and with anisotropy values ρ equivalent to $\hat{\lambda}_h/\hat{\lambda}_z$ from the MC results. Assuming that the MC results are accurate and can be adequately modelled by the second-order expression (13), then the difference between the K_{eff} values from the MC simulations and the K_x values from (12), appropriately evaluated, is a simple linear function of the second-order correction factor γ_{11}. Values for the γ_{11} correction factor, so derived, are plotted in Figure 8; a quadratic polynomial has been fit to this data. Using this quadratic polynomial as an estimate of γ_{11}, (13) was evaluated and the result plotted on Figure 7 (solid line). Note that the $-2\gamma_{11}$ values thus derived are considerably smaller than those given by *Indelman and Abramovich* [1994, their Figure 4]; indeed, the values here are even smaller than that found in the σ_f^2 scenario above. To obtain more precise estimates of these γ_{11} values, by MC simulation, one would need many more realizations than used in this study. In general, results from both the σ_f^2 and the statistical anistropy scenarios strongly suggest that the *Indelman and Abramovich* [1994] correction factor is viable and is an important aspect of the effective hydraulic conductivity when σ_f^2 is large. These MC simulations also indicate that their analytical results may overestimate the strength of the correction factor but, given the quality of the MC results (the statistical anistropy scenario in particular), this can only be conjuctured.

Plume Velocity

In most subsurface transport studies, the mean plume velocity, about which spreading occurs, is assumed to be equivalent to the mean seepage velocity of the flow system. Some investigators have indicated that this assumption may be overly simplistic (see, e.g., *Freeze and Cherry* [1979, p.71]); the purpose of this section is to present whatever evidence concerning this assumption that these MC simulations may provide. MC simulations of tracer migration were performed in association with the two flow scenarios presented in the previous section; the plume was started from an initial box near the upstream end of the flow cells. The centroid velocity, V_c, of each plume realization was obtained from the late-time portion of the x-direction first-moment curves; the technique used to obtain these moments is detailed in the companion paper [*Naff et al.*, this issue] and the method used to derive velocities from these moment curves is detailed in the next section. The mean centroid velocity, $\langle V_c \rangle$, is estimated from these individual realization plume velocities, as is the standard deviation of V_c. The mean seepage velocity, $\langle V_x \rangle$, can be estimated directly from the mean specific discharge $\langle q_x \rangle$ by dividing by the porosity (assumed constant in this study).

Mean centroid plume and seepage velocities, as a function of variance in log hydraulic conductivity, are depicted in Figure 9. The estimated statistical anisotropy for this case is $\hat{\lambda}_h/\hat{\lambda}_z = 10.0$ and local dispersivities are maintained at $\alpha_\ell = 0.1\ m$ and $\alpha_t = 0.01\ m$. These results indicate that the ensemble average cloud centroid velocity is slightly smaller than the mean seepage velocity; the ratio of the two velocities $\langle V_x \rangle / \langle V_c \rangle$ varies from 1.01 for the smaller value of $\hat{\sigma}_f^2$ to 1.05 for the largest value of $\hat{\sigma}_f^2$. The error bars on this figure represent the standard error for the statistic $\langle V_x \rangle - \langle V_c \rangle$; using the standard error for this difference statistic, rather than $\langle V_c \rangle$ and $\langle V_x \rangle$ separately, allows for the incorporation of variability from both sources into a single standard error estimate (placement of the error bar on $\langle V_c \rangle$ rather than $\langle V_x \rangle$ is arbitrary). These error bars indicate that the difference in the

two means depicted in Figure 9 are only marginally significant. More directly, by assuming that V_c and V_x themselves are normally distributed, one can use the t statistic to estimate the significance of these differences. Under the hypothesis that $\langle V_c \rangle$ and $\langle V_x \rangle$ are identical, then the probability of obtaining a difference this large or larger from simple random variation ranges from 0.28, for $\hat{\sigma}_f^2 = 0.437$, to 0.35, for $\hat{\sigma}_f^2 = 0.874$. While these probabilities are small, they are not so small that one could consider it improbable that these means are identical. Because of the small magnitude in the differences between $\langle V_x \rangle$ and $\langle V_c \rangle$ plus the marginal significance of these differences for this scenario, it is not possible to state explicitly that the $\langle V_x \rangle$ and $\langle V_c \rangle$ are truly different means.

Mean plume and seepage velocities as a function of statistical anisotropy are presented in Figure 10. The estimated variance in log hydraulic conductivity for this case is $\hat{\sigma}_f^2 = 0.443$; the local dispersivities remain fixed at $\alpha_\ell = 0.1\ m$ and $\alpha_t = 0.01\ m$. Here, for the smallest anisotropy ratio ($\hat{\lambda}_h/\hat{\lambda}_z = 4.96$), the difference between $\langle V_x \rangle$ and $\langle V_c \rangle$ does appear to be significant as the error bar for $\langle V_c \rangle$ does not include the $\langle V_x \rangle$ data (the error bars are again based on the standard error of the difference statistic $\langle V_x \rangle - \langle V_c \rangle$); the ratio of $\langle V_x \rangle$ to $\langle V_c \rangle$ is 1.06 for this anisotropy value. However, $\langle V_x \rangle$ and $\langle V_c \rangle$ are essentially identical when the anisotropy ratio is 9.92 or greater, indicating that, if any differences do exist, they are associated with smaller anisotropy ratios. Note that, in contrast to Figure 9, the widths of the error bars are nearly constant for all values of $\hat{\lambda}_h/\hat{\lambda}_z$. A trend toward a difference in $\langle V_x \rangle$ and $\langle V_c \rangle$ with smaller anisotropy ratios is not hampered by ever larger error bars. Using a t statistic and given the hypothesis that $\langle V_x \rangle$ and $\langle V_c \rangle$ are equal, the probability of obtaining, from simple random variation, a difference as large or larger than those observed is 0.21 for the ratio $\hat{\lambda}_h/\hat{\lambda}_z = 4.92$. For $\hat{\lambda}_h/\hat{\lambda}_z = 6.62$, this probability increases to 0.49 and is nearly one for the larger ratios.

Figure 9 and 10 do share one data location in common: $\hat{\lambda}_h/\hat{\lambda}_z \approx 10$ and $\hat{\sigma}_f^2 \approx 0.44$. For Figure 9, the estimated values of $\langle V_x \rangle$ and $\langle V_c \rangle$ are 0.0991 m/d and 0.0953 m/d, respectively. For Figure 10, the equivalent estimated values are both 0.0972 m/d. One would expect that, as the number of realizations for both scenarios approached infinity, both $\langle V_x \rangle$ and $\langle V_c \rangle$ would take on values corresponding to their equivalent population parameters ($\langle V_x \rangle$ and $\langle V_c \rangle$ are simply statistics with their appropriate distributions). Thus, the differences exhibited here between the two values for $\langle V_x \rangle$ and between the two values for $\langle V_c \rangle$ can be attributed to variation associated with a 20 realization MC simulation. The $\langle V_x \rangle$ data presented in Figures 9 and 10 are the basis for the effective hydraulic conductivity results presented in the previous section; these results, which generally produce good fits with first-order approximations, suggest that the $\langle V_x \rangle$ results are reasonable representations of the mean seepage velocity. That $\langle V_x \rangle$ and $\langle V_c \rangle$ do agree over a considerable range in Figure 10 does inspire some confidence that these results might be representative of their true means, even though the error bars are large.

If a difference between $\langle V_x \rangle$ and $\langle V_c \rangle$ exists, it is probably small, being on the order of 5% or less. Because the effect being sought (should it exist) is likely to be small and the error bars are large, no absolute resolution as to whether $\langle V_x \rangle$ and $\langle V_c \rangle$ are equivalent or different is available from this study. For the scenario where the variance in log hydraulic conductivity was allowed to vary, because of the marginal significance of the difference between $\langle V_x \rangle$ and $\langle V_c \rangle$, it is not possible to state explicitly that the observed differences are significant. On the other hand, for the scenario where the statistical anisotropy was allowed to vary, there is evidence for both the equivalency of $\langle V_x \rangle$ and $\langle V_c \rangle$ (large anisotropy ratios) and for a significant difference between $\langle V_x \rangle$ and $\langle V_c \rangle$ (small anisotropy ratios). Only when the statistical anisotropy is small does it appear possible that $\langle V_x \rangle$ is significantly different from $\langle V_c \rangle$. This latter observation is somewhat bolstered by the relation of the error bars to the trend present in Figure 10. As the anisotropy ratio decreases, the difference

between $\langle V_x \rangle$ and $\langle V_c \rangle$ increases while the error bars remain approximately constant, suggesting that the difference should be significant at very small anisotropies.

Variance in Velocity of Plume Centroid

The primary objective of this section is to report on the effect of source-size thickness and local transverse dispersion on the variance in plume centroid velocity. With other parameters constant, work by *Dagan* [1990, 1991] suggests that the variance in plume velocity should decrease with increasing thickness of the source region box. The effect of source-size thickness on the variance in plume centroid velocity was examined using a flow cell which was somewhat larger than normal in the z direction; the cell dimensions were $60 \times 15 \times 10.5\ m^3$; the z dimension of the source region box I_z was allowed to vary from 1/8 meter to one meter. The effective length scales of the medium were $\hat{\lambda}_x = 2.78\ m$, $\hat{\lambda}_y = 2.79\ m$ and $\hat{\lambda}_z = 0.278\ m$; the mean variance in $f(\vec{x})$ was 0.512. Thus, the relative depth $I_z/\hat{\lambda}_z$ of the source box varies from 0.45 to 3.6. This range of source region thicknesses, which was basically forced by the memory restrictions of the modelling effort, suffices to give one an indication of the effect of source size.

The variance in plume centroid velocity is a function of the travel time of the plume. To illustrate this concept, a comparison between the mean plume centroid $\langle X_c \rangle$ in the x direction and the equivalent centroid of an individual realization plume X_c is shown in Figure 11 for the case where $I_z/\hat{\lambda}_z = 0.45$. Note that the 20 realization mean centroid $\langle X_c \rangle$ profile is somewhat shorter than the single-realization X_c result. One or more plume realizations encountered the detection boundary before the end of the 300 day limit of the simulation; a complete 20 realization suite is available only to day 260 of the simulation. In this study, the mean plume velocity $\langle V_c \rangle$ in the x direction is defined as the slope of a straight-line fit to the late-time $\langle X_c \rangle$ data, as indicated in this figure. An estimate of the centroid velocity for a single realization can be obtained by fitting a straight line to the single-realization profile over the same time period as that used in the mean profile (in this case, 60 to 260 days). The mean, over all realizations, of these approximate centroid velocities is essentially identical to the mean velocity obtained from fitting the $\langle X_c \rangle$ profile

directly; these approximate, individual realization plume velocities are useful for evaluating the standard error (estimates of the standard error for $\langle V_x \rangle - \langle V_c \rangle$ of the previous section use these individual realization estimates for V_c). However, this procedure obviously doesn't capture the temporal aspect of the variation in V_c. To capture this aspect of the velocity variation, individual realization X_c data were differenced to approximate V_c as a function of time; for every time step, the variance of V_c was then estimated across the 20 realizations of the simulation. These results, plotted as the coefficient of variation for $V_c(t)$, are presented in Figures 12: Figure 12a depicts the result for $I_z/\hat{\lambda}_z = 0.45$ and Figure 12b is for $I_z/\hat{\lambda}_z = 3.6$. The coefficient of variation for $V_c(t)$ decreases by a factor of two over the 10 length scales $\hat{\lambda}_x$ of travel time shown in these figures; the rate of decrease appears to moderate near the end of the simulation travel time. The straight-line slope method of approximating an average variance for V_c produces a coefficient of variation which agrees approximately with the late-time results of Figures 12a and 12b. Thus, while the straight-line slope approximation does not capture the temporal variation in plume velocity, it does provide, for the simulation period in question, a representative measure of the variation in centroid velocity. This approximate measure of the variation in V_c is used in this study to evaluate the effect of source size on the variation in V_c; similar measures are used in the companion paper [*Naff et al.*, this issue] to estimate variability in certain macrodispersive properties of the plume.

The coefficient of variation for V_c, based on the straight-line slope approximation, as a function of relative source thickness $I_z/\hat{\lambda}_z$ is shown in Figure 13. This measure for the variance in V_c suggests that, as indicated indirectly by *Dagan* [1990, 1991], the variation in V_c does decrease with increasing source size perpendicular to the direction of flow; the rate of decrease however is rather slow. If one hazards to extrapolate the best-fit quadratic line to these data, then a minimum source size of about 20 length scales λ_z would be necessary

before the coefficient of variation depicted in Figure 13 becomes essentially null. This result indicates that, before one can expect a field plume to move with a nearly constant velocity consistent with its mean, the tracer cloud should be injected over at least 20 length scales λ_z. The importance of this variation in V_c not only lies in how closely V_c approaches $\langle V_c \rangle$, but also in that this variation in the mean plume velocity causes the mean cloud to have an enhanced apparent dispersion; this enhanced apparent dispersion is discussed in the companion paper.

The effect of local transverse dispersion on the variance in plume centroid velocity was examined using a flow cell whose lateral dimensions were enlarged to accommodate a range of local transverse dispersivities without otherwise altering the MC simulation; these dimensions were $60 \times 19.5 \times 14.5\ m^3$. The effective length scales of the generated medium were $\hat{\lambda}_x = 2.78\ m$, $\hat{\lambda}_y = 2.79\ m$ and $\hat{\lambda}_z = 0.278\ m$; the mean variance in $f(\vec{x})$ was 0.527. The transverse dispersivities α_t were allowed to vary from $0.005\ m$ to $0.05\ m$; the relative transverse dispersivity $\alpha_t/\hat{\lambda}_z$ varied from 0.018 to 0.18. The longitudinal component α_ℓ was held constant at $0.1\ m$. The variance in V_c was again approximated using the straight-line slope approximation with an estimation interval from 75 to 250 days; $\langle V_c \rangle$ was very nearly constant at $0.102\ m/d$ for all values of $\alpha_t/\hat{\lambda}_z$. The results of this investigation, depicted in Figure 14, indicate that, when the plume undergoes increased lateral spreading through increased values of the local transverse dispersivity, the variance in centroid velocity is diminished. Increasing $\alpha_t/\hat{\lambda}_z$ by a factor of ten decreases the coefficient of variation by a factor less than 2. Local transverse dispersion apparently has the effect of spreading the cloud over an ever greater volume and thus averaging more of the velocity field into the plume migration. It is probable that the decrease in the coefficient of variation with plume travel shown in Figure 12 is attributable to a similar phenomena; that is, as the tracer cloud grows laterally in response to local transverse dispersion, it encompasses more of the heterogeneous formation; this lateral smearing of the plume decreases the overall variability in V_c in a manner

similar to that of increasing in the lateral dimension of the injection zone. Increasing α_t independently of the hydraulic conductivity K, as done here, is not entirely realistic; α_t and K are likely to be related in most field situations and thus an increase in the mean of one should be accompanied by an increase in the mean of the other. Here we only attempt to demonstrate the effect α_t has on the variance in cloud velocity.

Concluding Remarks

Estimation of length scales for a given covariance model from either artificially generated random fields or from actual field data is a difficult problem. Because common covariance functions or variogram estimators produce unreasonable estimates for large lags, and as the influence of these large-lag estimates increases with increased dimensionality of the problem, the usual least-squares approximation techniques produce poor estimates of these quantities. A data censoring technique, or a weighted least-squares approximation similar to that suggested by [*Cressie*, 1991], may be necessary to produce reasonable estimates of length scales in two and three dimensions.

The second-order approximation for the effective hydraulic conductivity, as conceived by *Indelman and Abramovich* [1994], shows general agreement with the Monte-Carlo simulation results obtained in this study. The presence of a correction factor, γ_{11}, in the second-order term appears to be necessary, although their theoretical results may overstate this factor. The shape of the correction factor, as given by *Indelman and Abramovich* [1994], agrees generally with the Monte-Carlo simulation results, although this agreement could be serendipitous because of the large standard errors associated with the statistical anisotropy senario.

To determine whether the differences found in this study between the mean plume centroid velocity and the mean seepage velocity are significant, Monte-Carlo simulations with more realizations than used herein are needed. This is somewhat problematic since, in order to decrease the standard error of these estimated means by a factor of two, four times as many realizations will be necessary (a reduction by at least a factor of two would be desirable). With these current results, one can only posit that, when the statistical anisotropy λ_h/λ_z is small, $\langle V_c \rangle$ is likely to be smaller than $\langle V_x \rangle$. That is, it is to be expected

that the the mean velocity of the plume will be slightly retarded relative to the mean seepage velocity as the medium heterogeneity causes the fluid to deviate further from the mean flow path. If the very tentative results of Figure 9 were to be believed, then this effect would be enhanced by increasing the variance in the log hydraulic conductivity.

An ancillary conclusion from the comparison between $\langle V_c \rangle$ and $\langle V_x \rangle$ concerns the poor correspondence of results between different scenarios in which each scenario contains a common parameter set. Monte-Carlo simulations for the variance in hydraulic conductivity and the statistical anisotropy scenarios (Figures 9 and 10) were run with independent sets of random fields $K(\vec{x})$, but with one 20 realization Monte-Carlo simulation from each having common input parameters. The poor correspondence of results for these two simulations indicates that it is desirable to increase the number of realizations in these Monte-Carlo simulations significantly so as to obtain a better correspondence. With the 20 realization simulations used herein, it is possible to detect trends within any one scenario (provided the set of generated $K(\vec{x})$ fields do not change from case to case within the scenario), but comparisons between scenarios, with independent $K(\vec{x})$ fields, were not of the quality that we had sought. This effect is also apparent from simulations presented in the companion paper [*Naff et al.*, this issue].

The lateral dimension of a tracer plume, relative to the average size of a heterogeneity within the medium, is an important element in controlling the relative variance of the centroidal velocity of the plume. For these simulations, it was found that the standard deviation of the plume velocity for any realization, as determined by fitting a straight line to a plot of the advance of the x-direction centroid versus time, was on the order of 0.1 times the mean centroidal velocity. As the plume becomes larger, either by injection over a larger volume or by natural growth resulting from transverse dispersion, then it is to be expected that the variance will be yet further reduced (it is considered likely that most

naturally occurring plumes will cover many more vertical length scales than allowed in these simulations). That plume velocities determined by the best-fit straight-line approximation method should have such small coefficients of variation suggests that the centroidal velocity, as determined from a field tracer test and by a similar method, should be a reasonable estimate of the overall mean plume velocity. As a consequence, one can speculate that inverse methods which use the motion of a tracer cloud as an observation should also capture the mean plume and ground-water velocity relatively well.

Acknowledgments

We wish to thank the National Center for Atmospheric Research at Boulder, Colorado, for having given us time on a Cray-3 supercomputer; without this resource, it is unlikely that this study could have been completed. We also wish to thank all the former employees of Cray Computer Corporation for all the assistance lent to make our model work efficiently on this machine. Gilbert Barth and Steen Christensen provided critical reviews in early drafts of this two-part paper.

References

Bellin, A., P. Salandin, and A. Rinaldo, Simulation of dispersion in heterogeneous porous formations, *Water Resour. Res.*, 28(9), 2211-2227, 1992.

Burr, D.T., *Numerical investigations of solute transport in three-dimensional heterogeneous media*, M.Sc. thesis, 95 pp., Univ. of Waterloo, Waterloo, Ont., Canada, 1992

Burr, D.T., E.A. Sudicky and R.L. Naff, Nonreactive and reactive solute transport in three-dimensional heterogeneous media: Mean displacement, plume spreading and uncertainty, *Water Resour. Res.*, 30(3), 791-815, 1994.

Carle, S.F., and G.E. Fogg, Transition probability-based indicator geostatistics, *Mathematical Geology*, 28(2), 1996.

Cai, Z., J.E. Jones, S.F. McCormick and T.F. Russel, Control-Volume Mixed Finite Element Methods, submitted to *Computational Geosciences*, 1997

Chin, D.A., and T. Wang, An investigation of first-order stochastic dispersion theories in isotropic porous media, *Water Resour. Res.*, 28(6), 1531-1542, 1992.

Cressie, N.A.C., *Statistics for Spatial Data*, John Wiley, 900p., 1991.

Dagan, G., Stochastic modeling of groundwater flow by unconditional and conditional probabilities, 1, Conditional simulation and the direct problem, *Water Resour. Res.*, 18(4), 813-833, 1982.

Dagan, G., Solute transport in heterogeneous porous formations, *J. Fluid Mech.*, 145, 151-177, 1984.

Dagan, G., Time-dependent Macrodispersion for solute transport in anisotropic heterogeneous aquifers, *Water Resour. Res.*, 24(9), 1491-1500, 1988.

Dagan, G., Transport in heterogeneous porous formations: spatial moments, ergodicity, and effective dispersion, *Water Resour. Res.*, 26(6), 1281-1290, 1990.

Dagan, G, Dispersion of a passive solute in non-ergodic transport by steady velocity fields in heterogeneous formations, *J. Fluid Mech.*, 233, 197-210, 1991.

de Hoog, F.R., J.H. Knight, and A.N. Stokes, An improved method for numerical inversion of Laplace transforms, *SIAM J. Sci. Stat. Comput.*, 3(3), 357-366, 1982.

Freeze, R.A., and J.A. Cherry, *Groundwater*, Prentice-Hall, 604p., 1979.

Gelhar, L.W., and C.L. Axness, Three-dimensional stochastic analysis of macrodispersion in a stratified aquifer, *Water Resour. Res.*, 19(1), 161-180, 1983.

Indelman, p., and B. Abramovich, A higher-order approximation to effective conductivity in media of anisotropic structure, *Water Resour. Res.*, 30(6), 1857-1864, 1994.

Jussel, P., F. Stauffer, and T. Dracos, Transport modeling in heterogeneous aquifers: 1. Statistical description and numerical generation of gravel deposits, *Water Resour. Res.*, 30(6), 1803-1817, 1994a.

Jussel, P., F. Stauffer, and T. Dracos, Transport modeling in heterogeneous aquifers: 2. Three-dimensional transport model and stochastic numerical tracer experiment, *Water Resour. Res.*, 30(6), 1819-1831, 1994b.

Naff, R.L., and A.V. Vecchia, Stochastic analysis of three-dimensional flow in a bounded domain, *Water Resour. Res.*, 22(5), 695-704, 1986.

Naff, R.L., D.F. Haley and E.A. Sudicky, High-resolution Monte-Carlo simulation of flow and conservative transport in heterogeneous porous media: 2, transport results, *Water Resour. Res.*, this issue.

Percival, D.B., Three curious properties of the sample variance and autocovariance for stationary process with unknown mean, *The American Statistician* 47(4), 274-276, 1993.

Priestly, M.B., *Spectral Analysis and Time Series*, Academic Press, London, 890p. 1981.

Robin, M.J.L., A.L. Gutjahr, E.A. Sudicky and J.L. Wilson, Cross-correlated random field generator with direct Fourier transform method, *Water Resour. Res.*, 29(7), 2385-2397, 1993.

Sudicky, E.A., The Laplace transform Galerkin technique: A time-continuous finite element theory and application to mass transport in groundwater, *Water Resour. Res.*, 25(8), 1833-1846, 1989.

Sudicky, E.A., and R.G. McLaren, The Laplace transform Galerkin technique for large-scale simulation of mass transport in discretely fractured porous formations, *Water Resour. Res.*, 28(2), 499-514, 1992.

Tompson, A.F.P., Numerical simulation of chemical migration in physically and chemically heterogeneous porous media, *Water Resour. Res.*, 29(11), 3709-3726, 1993.

Tompson, A.F.P., and L.W. Gelhar, Numerical simulation of solute transport in three-dimensional, randomly heterogeneous porous media, *Water Resour. Res.*, 26(10), 2541-2562, 1990.

Webb, E.K., and M.P. Anderson, Simulation of preferential flow in three-dimensional, heterogeneous conductivity fields with realistic internal architecture, *Water Resour. Res.*, 32(3), 1996.

Figure Captions

Figure 1. Results of sample autocovariance function estimation problem. Dots represent mean of estimated ACF. Dashed and solid lines are results of using estimated length scale in x directions to evaluate equation (1): dashed represents weighted least squares estimate and solid represents spectral estimate.

Figure 2. Estimated normalized velocity variance, for y and z velocity components, in y direction (900 realization experiment).

Figure 3. Estimated normalized velocity variance, for y and z velocity components, in z direction (900 realization experiment).

Figure 4. Estimated normalized velocity variance, for y and z velocity components, in x direction (900 realization experiment).

Figure 5. Effect of initial region hydraulic conductivity on plume centroid location, X_c. Mean first moments, $\langle X_c \rangle$, for class intervals are depicted with punctate representation. Overall mean, $\langle\langle X_c \rangle\rangle$, is represented by solid line.

Figure 6. Effective hydraulic conductivity as a function of log hydraulic conductivity. Punctate representation: Monte-Carlo results. Solid line: quadratic fit to Monte-Carlo simulation results. Dashed line: first-order approximation, equation (8) with $K_\ell = 9.97$, $\rho = 10.0$.

Figure 7. Effective hydraulic conductivity as a function of statistical anisotropy. Punctate representation: Monte-Carlo results. Dashed line: first-order approximation (8). Solid line: second-order approximation (13) with γ_{11} from cubic polynomial, Figure 8.

Figure 8. Estimation of γ_{11} by polynomial fitting from statistical anisotropy scenario simulation results. Open circles: Monte-Carlo results. Solid line: quadratic fit.

Figure 9. Comparison of mean plume and mean elemental velocity as a function of log hydraulic conductivity. Punctate representation: Monte-Carlo results. Dashed lines: polynomial fit.

Figure 10. Comparison of mean plume and mean elemental velocity as a function of statistical anisotropy. Punctate representation: Monte-Carlo results. Dashed lines: polynomial fit.

Figure 11. Comparison of x-direction centroids: mean versus single realization.

Figure 12. Comparison of coefficients of variation for plume-centroid velocity. Punctate representation: from differencing X_c realization results. Dashed line: from straight-line fit to X_c realization results.

Figure 13. Coefficient of variation for plume-centroid velocity as a function of relative source thickness, $I_z/\hat{\lambda}_z$.

Figure 14. Coefficient of variation for plume-centroid velocity as a function of relative local transverse dispersivity, $\alpha_t/\hat{\lambda}_z$.

FIGURE 1

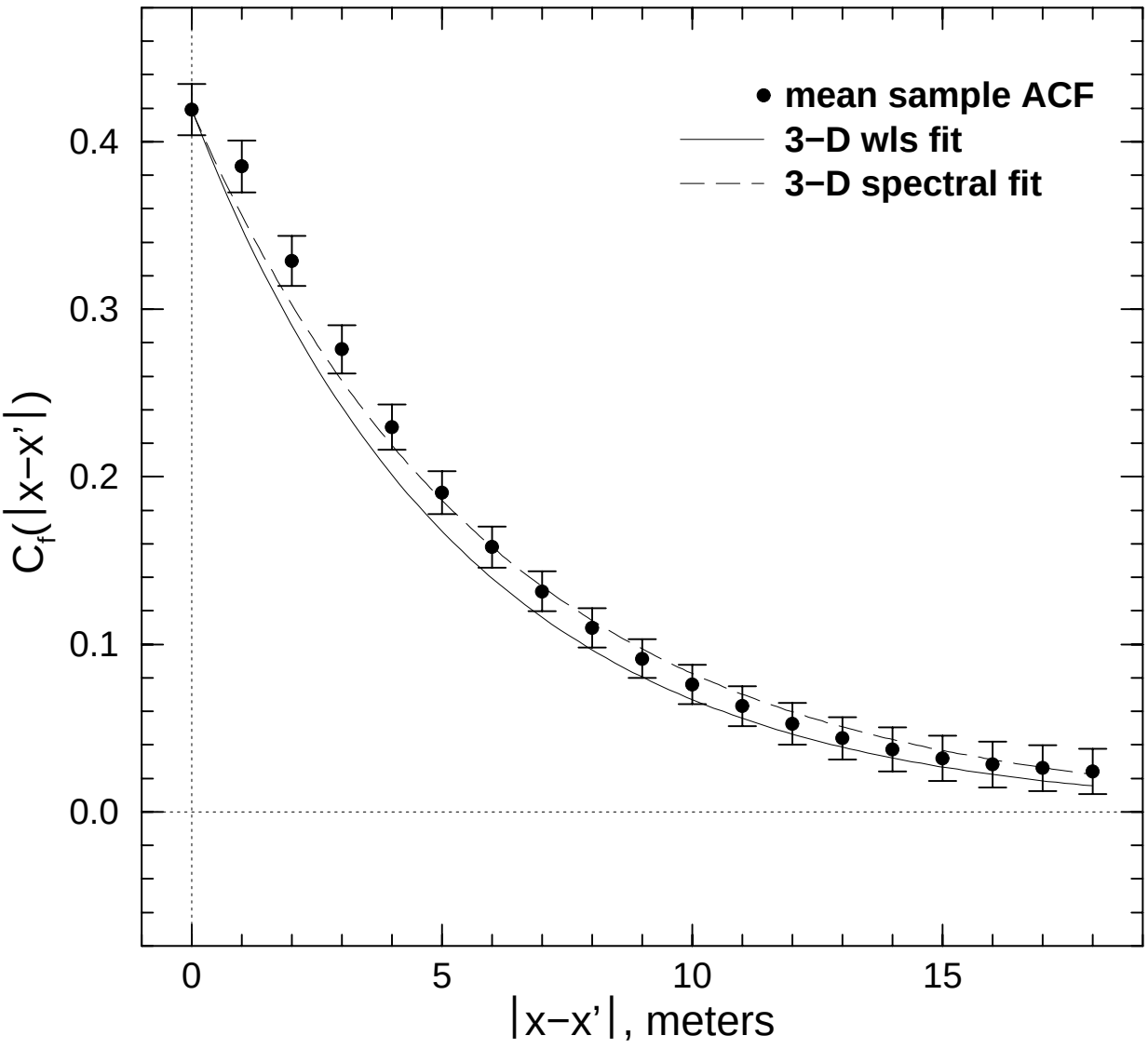
mean sample ACF
3−D wls fit
3−D spectral fit
0.4
0.3
0.2
0.1
0.0
$C_f(|x-x'|)$
0
5
10
15
$|x-x'|$, meters

FIGURE 2

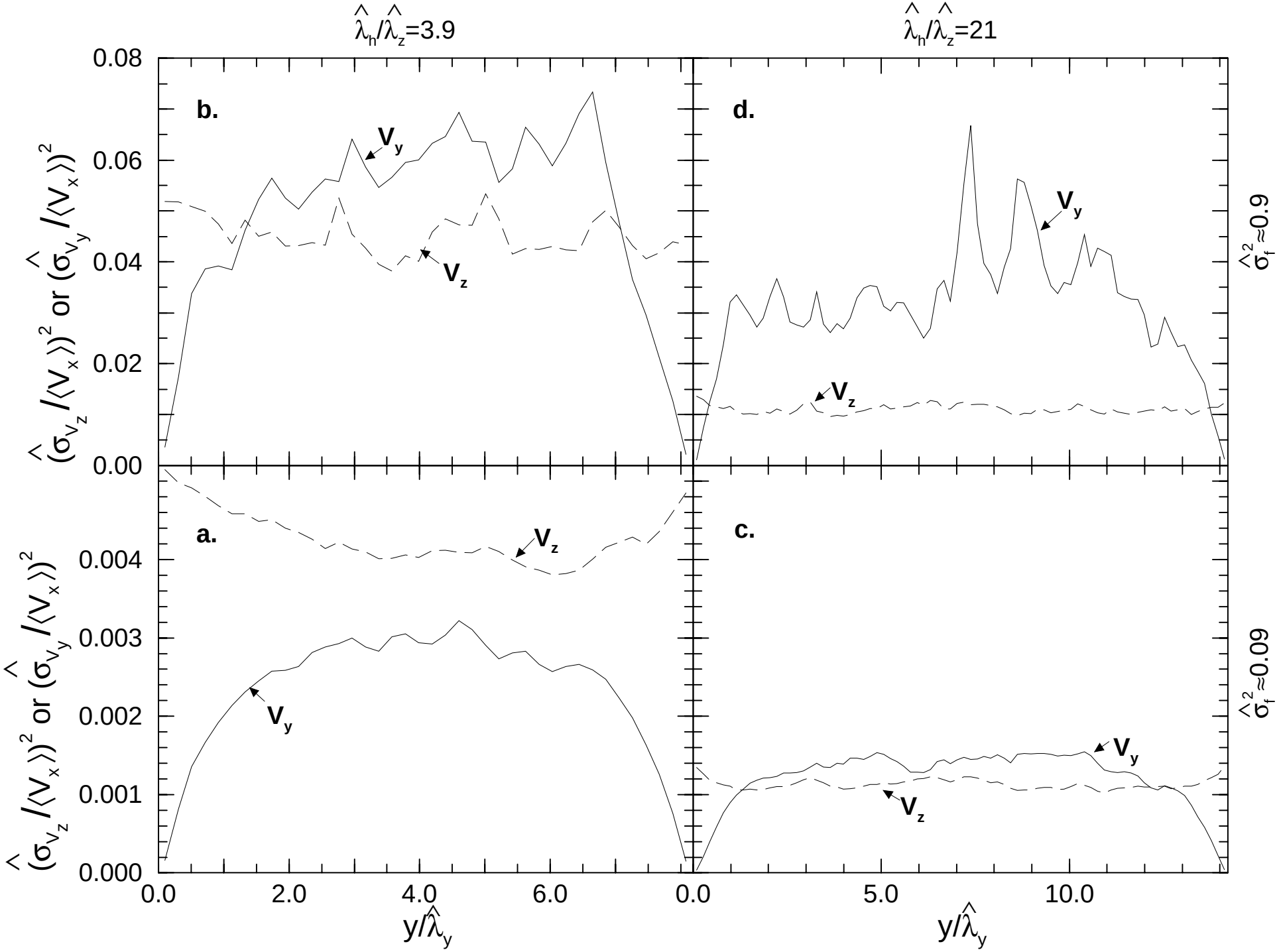
$\hat{\lambda}_h/\hat{\lambda}_z$=3.9
$\hat{\lambda}_h/\hat{\lambda}_z$=21
b.
d.
a.
c.
V_y
V_z
$\hat{\sigma}_f^2$≈0.9
$\hat{\sigma}_f^2$≈0.09
$\hat{(\sigma_{V_z}}/\langle V_x\rangle)^2$ or $\hat{(\sigma_{V_y}}/\langle V_x\rangle)^2$
$y/\hat{\lambda}_y$
0.08
0.06
0.04
0.02
0.00
0.004
0.003
0.002
0.001
0.000
0.0
2.0
4.0
6.0
5.0
10.0

FIGURE 3

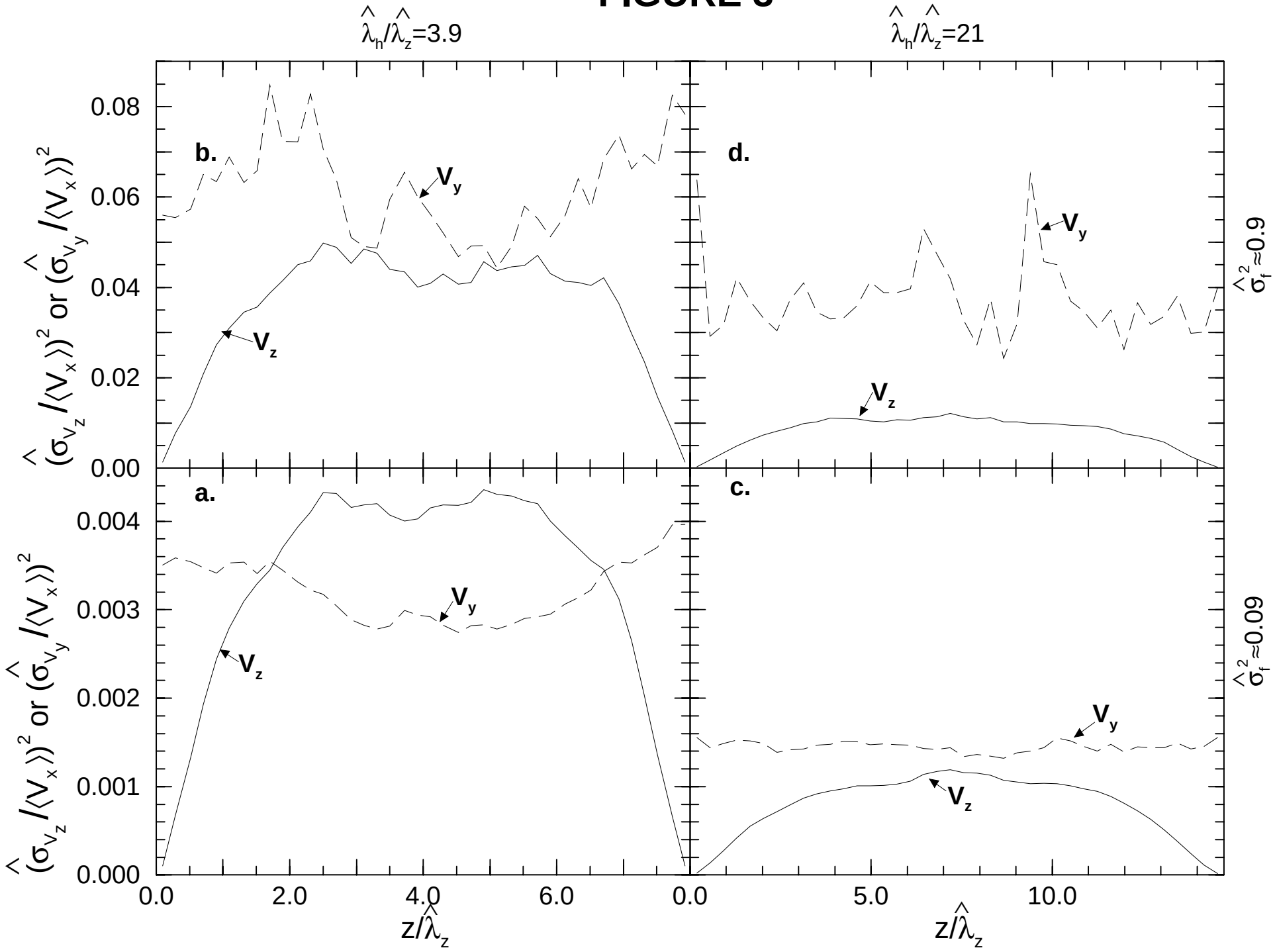
$\hat{\lambda}_h/\hat{\lambda}_z$=3.9
$\hat{\lambda}_h/\hat{\lambda}_z$=21
b.
d.
a.
c.
V_y
V_z
$\hat{\sigma}_f^2 \approx 0.9$
$\hat{\sigma}_f^2 \approx 0.09$
$\hat{(\sigma_{V_z}}/\langle V_x \rangle)^2$ or $\hat{(\sigma_{V_y}}/\langle V_x \rangle)^2$
$z/\hat{\lambda}_z$
0.08
0.06
0.04
0.02
0.00
0.004
0.003
0.002
0.001
0.000
0.0
2.0
4.0
6.0
5.0
10.0

FIGURE 4

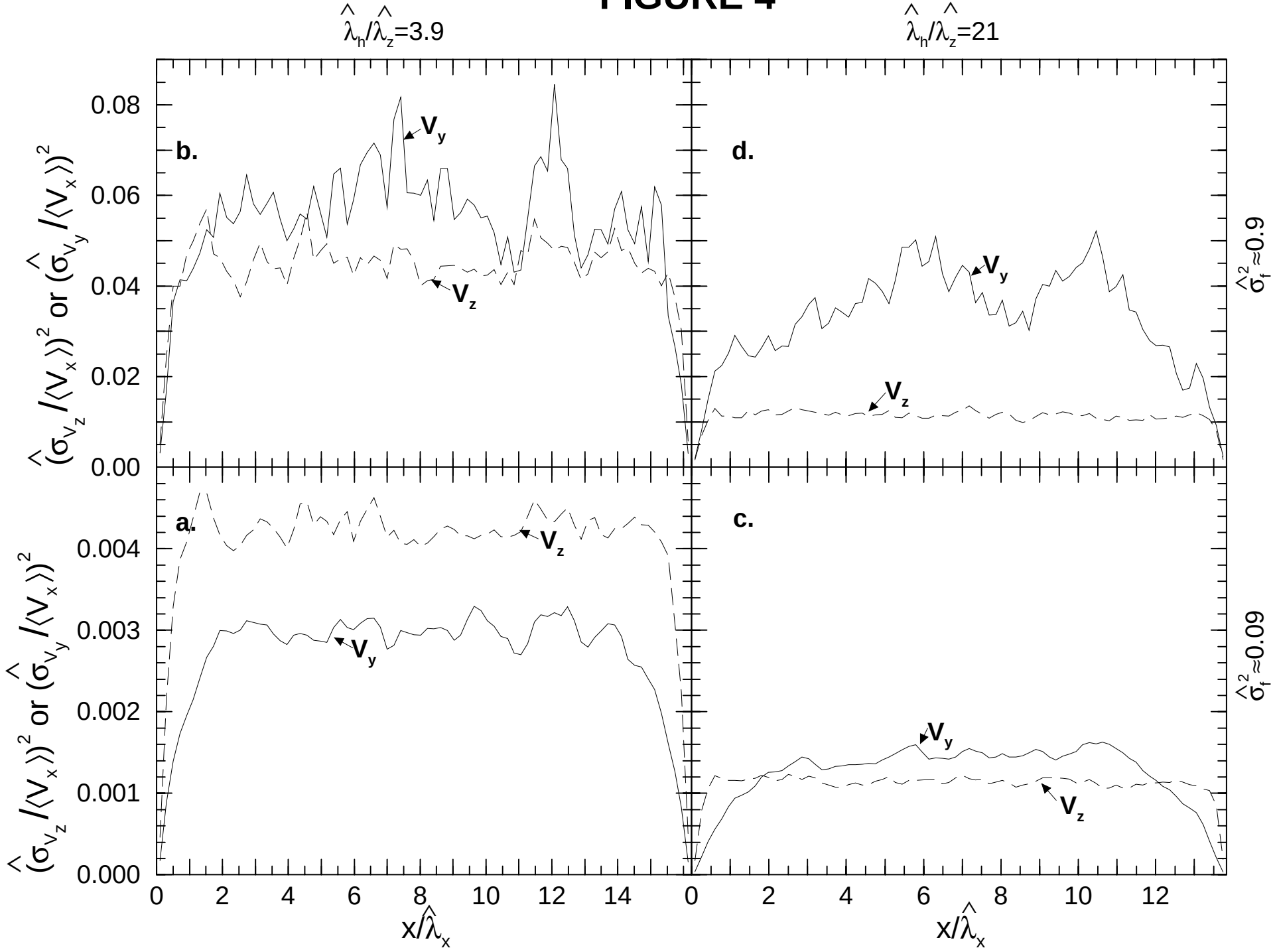
$\hat{\lambda}_h/\hat{\lambda}_z$=3.9
$\hat{\lambda}_h/\hat{\lambda}_z$=21
b.
d.
a.
c.
V_y
V_z
$\hat{\sigma}_{V_z}/\langle V_x\rangle)^2$ or $\hat{\sigma}_{V_y}/\langle V_x\rangle)^2$
$\hat{\sigma}_f^2 \approx 0.9$
$\hat{\sigma}_f^2 \approx 0.09$
$x/\hat{\lambda}_x$
0.08
0.06
0.04
0.02
0.00
0.004
0.003
0.002
0.001
0.000
0
2
4
6
8
10
12
14

FIGURE 5

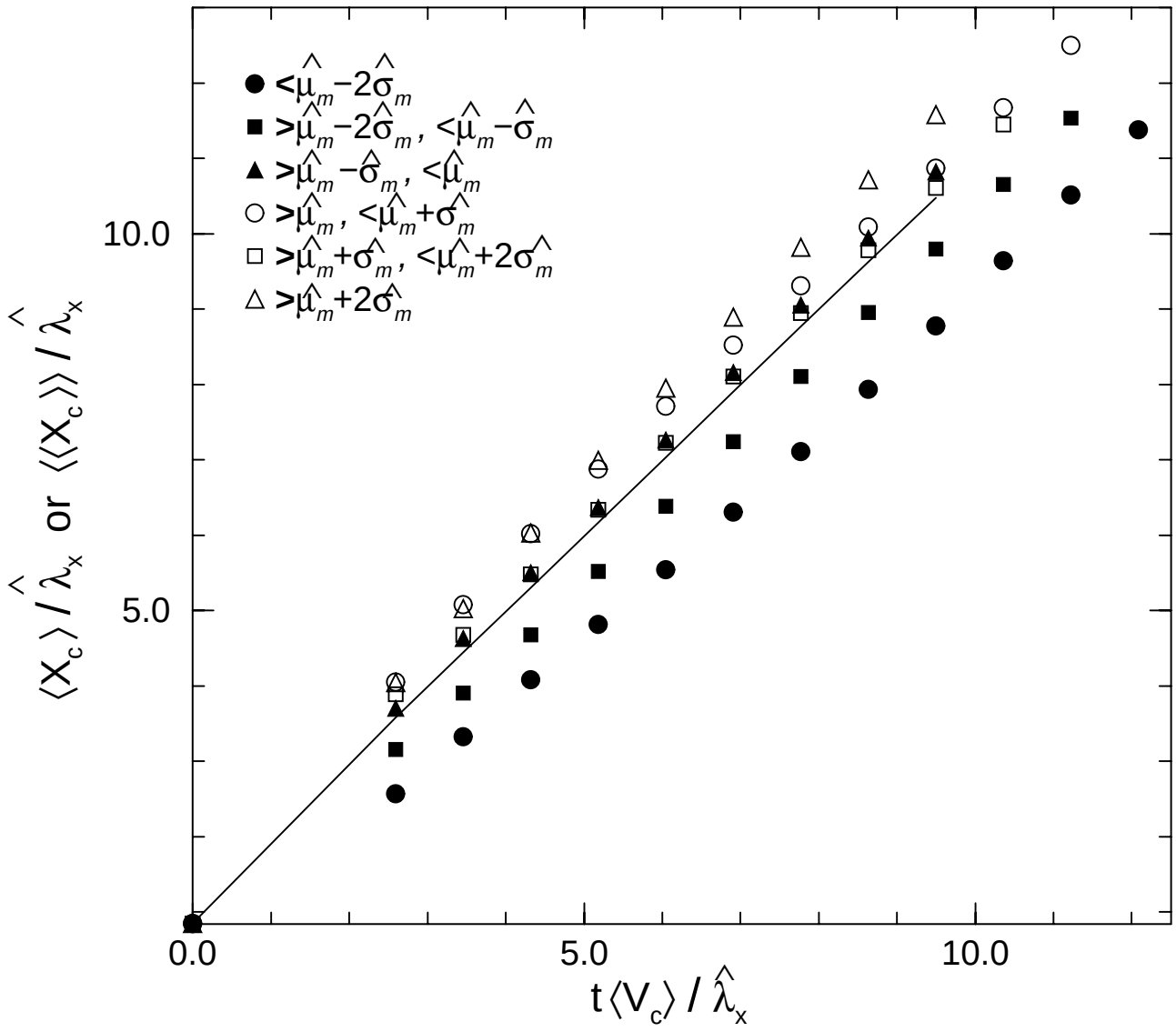
● <μ̂m−2σ̂m
■ >μ̂m−2σ̂m, <μ̂m−σ̂m
▲ >μ̂m−σ̂m, <μ̂m
○ >μ̂m, <μ̂m+σ̂m
□ >μ̂m+σ̂m, <μ̂m+2σ̂m
△ >μ̂m+2σ̂m
10.0
5.0
0.0
5.0
10.0
⟨Xc⟩ / λ̂x or ⟨⟨Xc⟩⟩ / λ̂x
t⟨Vc⟩ / λ̂x

FIGURE 6

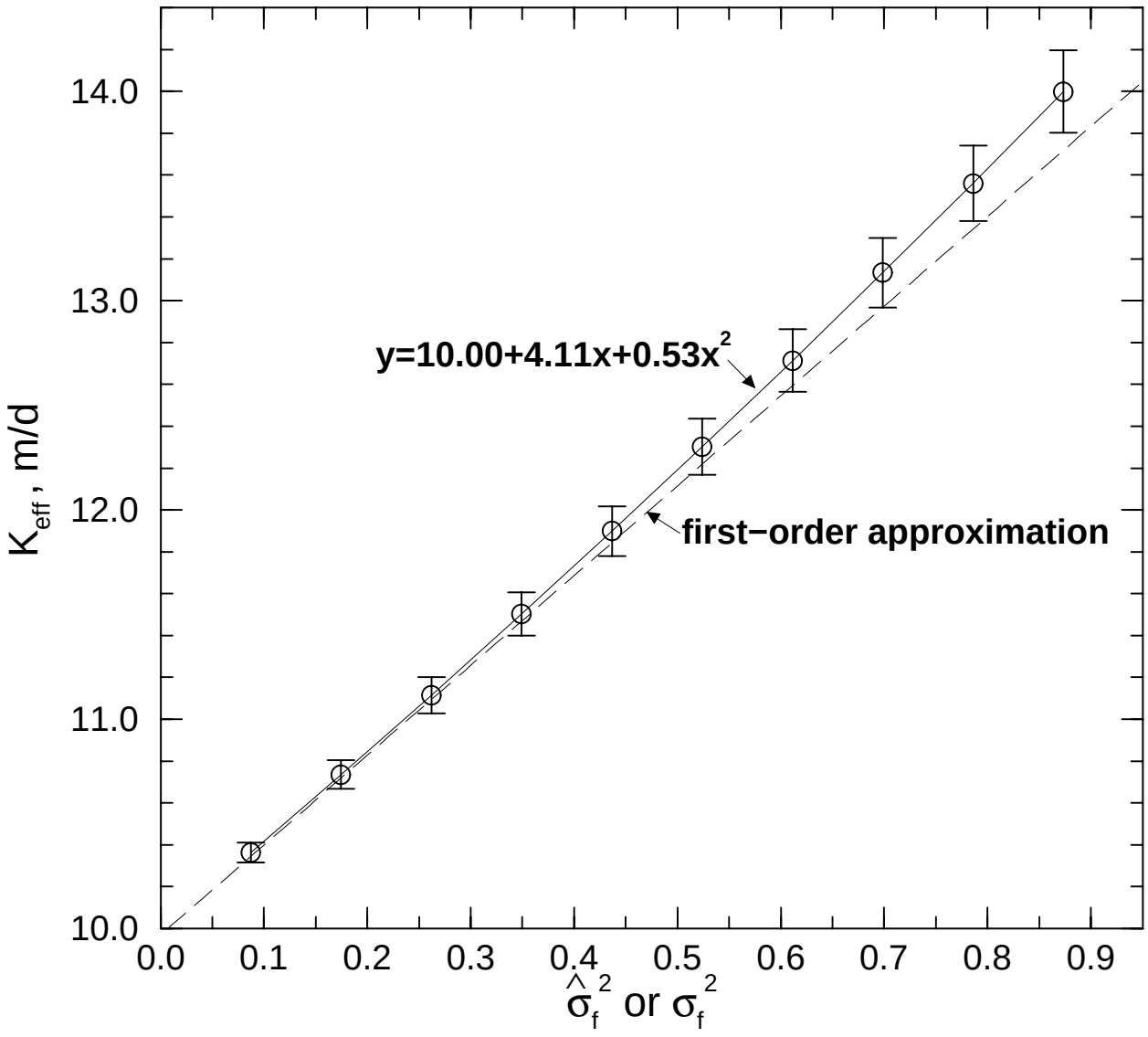
14.0
13.0
12.0
11.0
10.0
0.0
0.1
0.2
0.3
0.4
0.5
0.6
0.7
0.8
0.9
K_{eff}, m/d
$\hat{\sigma}_f^2$ or σ_f^2
y=10.00+4.11x+0.53x²
first−order approximation

FIGURE 7

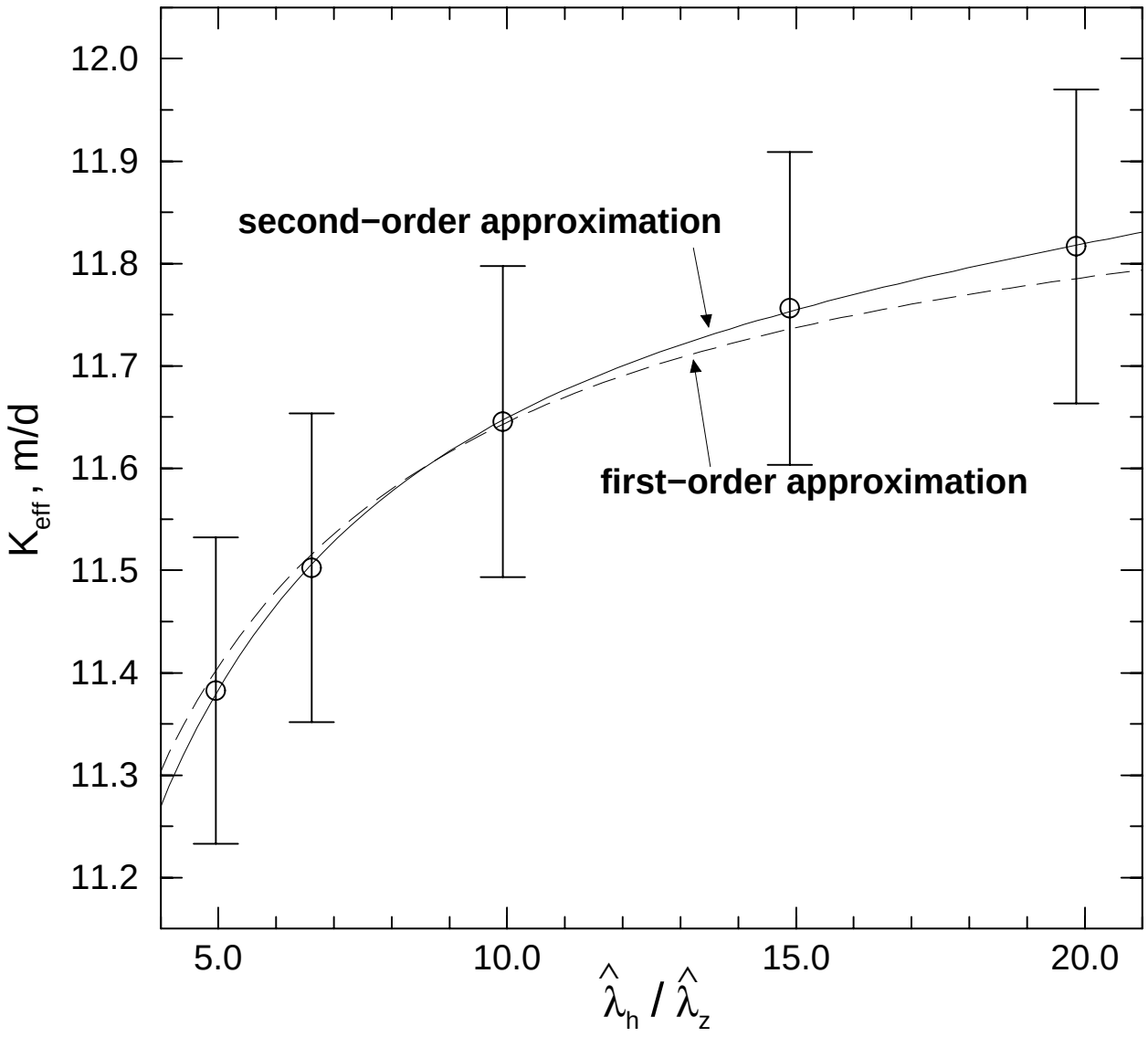
12.0
11.9
11.8
11.7
11.6
11.5
11.4
11.3
11.2
K_{eff}, m/d
second−order approximation
first−order approximation
5.0
10.0
15.0
20.0
$\hat{\lambda}_h / \hat{\lambda}_z$

FIGURE 8

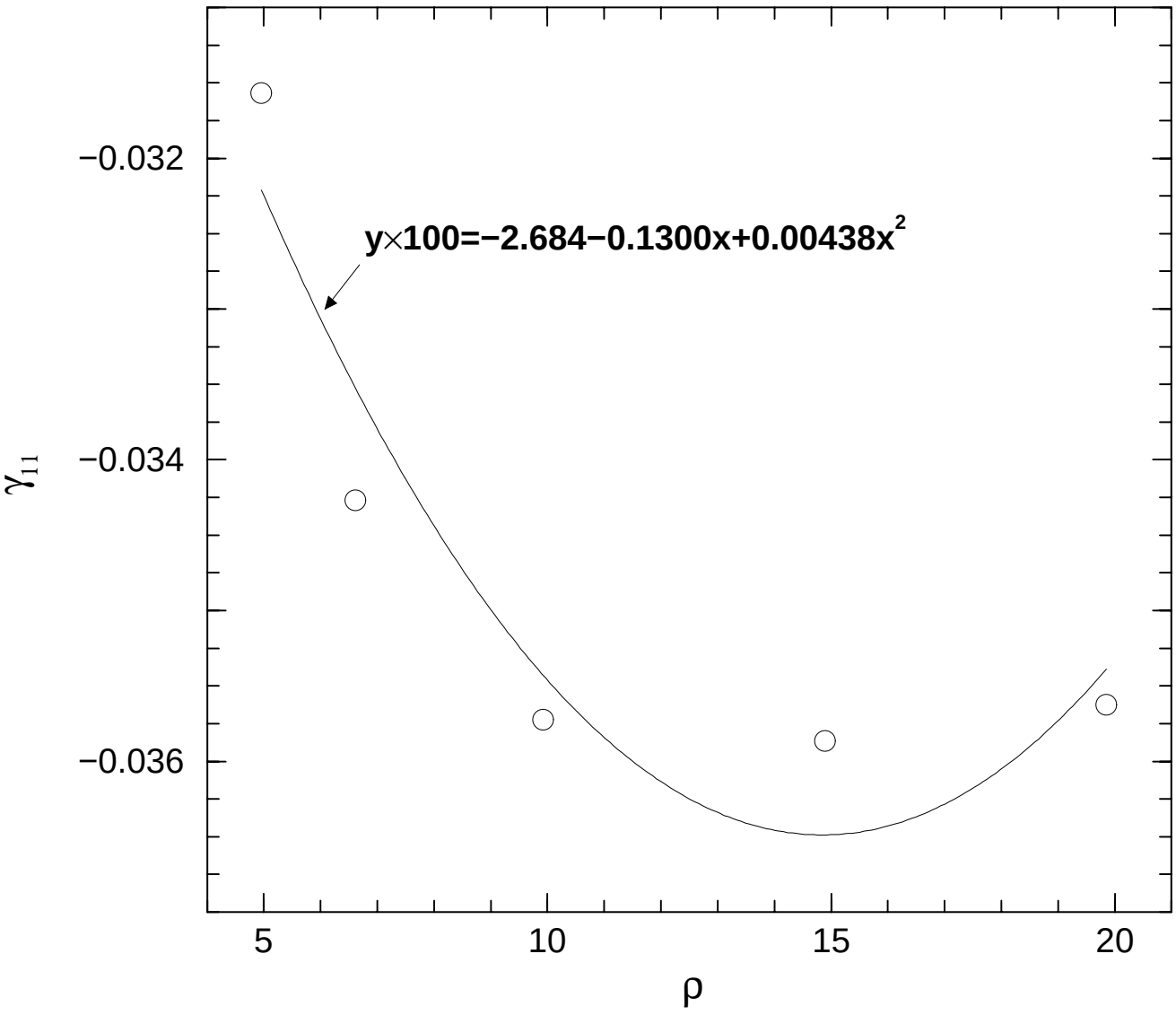

FIGURE 9

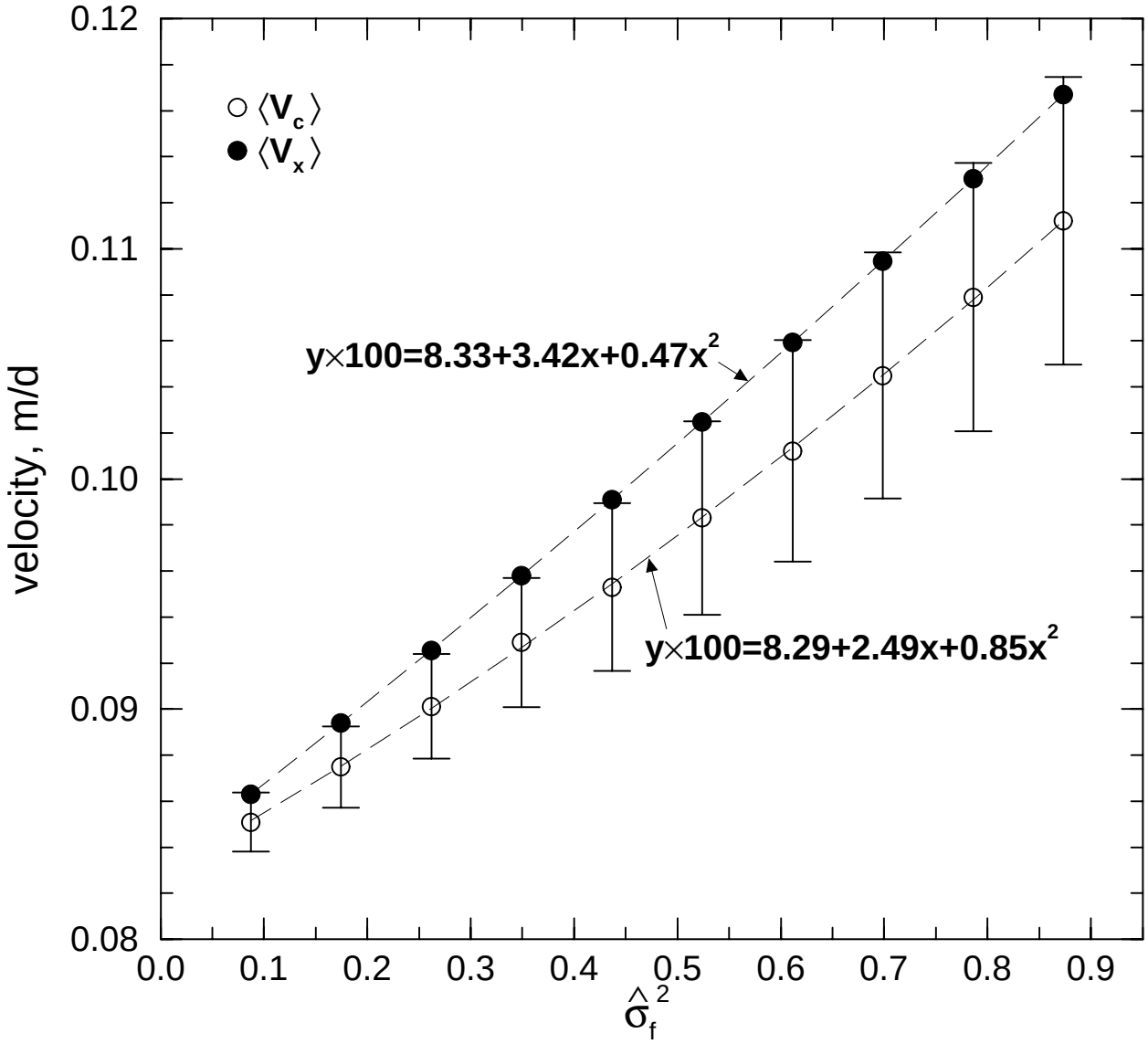
0.12
0.11
0.10
0.09
0.08
velocity, m/d
○ ⟨V_c⟩
● ⟨V_x⟩
y×100=8.33+3.42x+0.47x²
y×100=8.29+2.49x+0.85x²
0.0
0.1
0.2
0.3
0.4
0.5
0.6
0.7
0.8
0.9
σ̂_f²

FIGURE 10

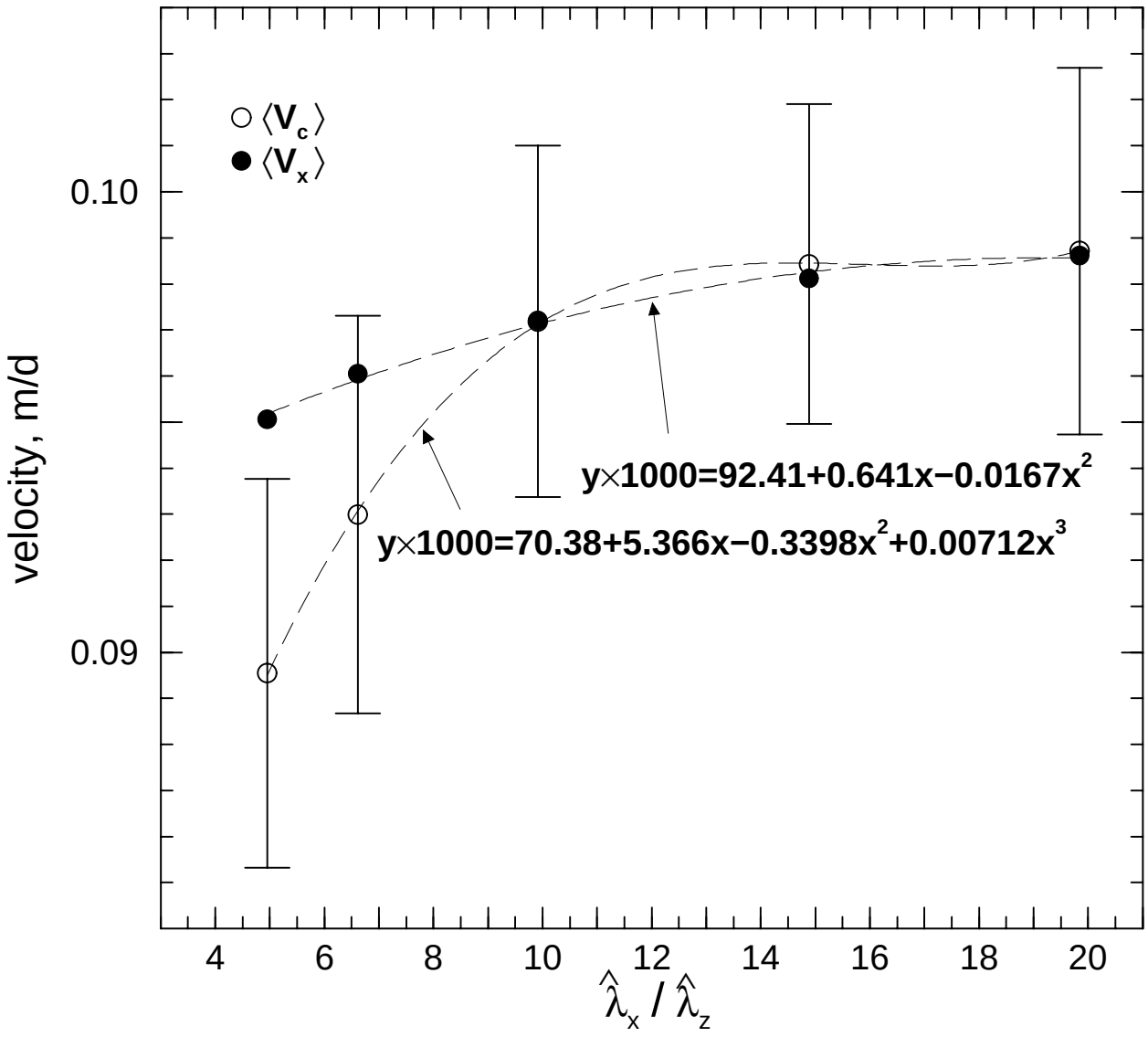
○ ⟨V_c⟩
● ⟨V_x⟩
0.10
0.09
velocity, m/d
y×1000=92.41+0.641x−0.0167x^2
y×1000=70.38+5.366x−0.3398x^2+0.00712x^3
4
6
8
10
12
14
16
18
20
λ̂_x / λ̂_z

FIGURE 11

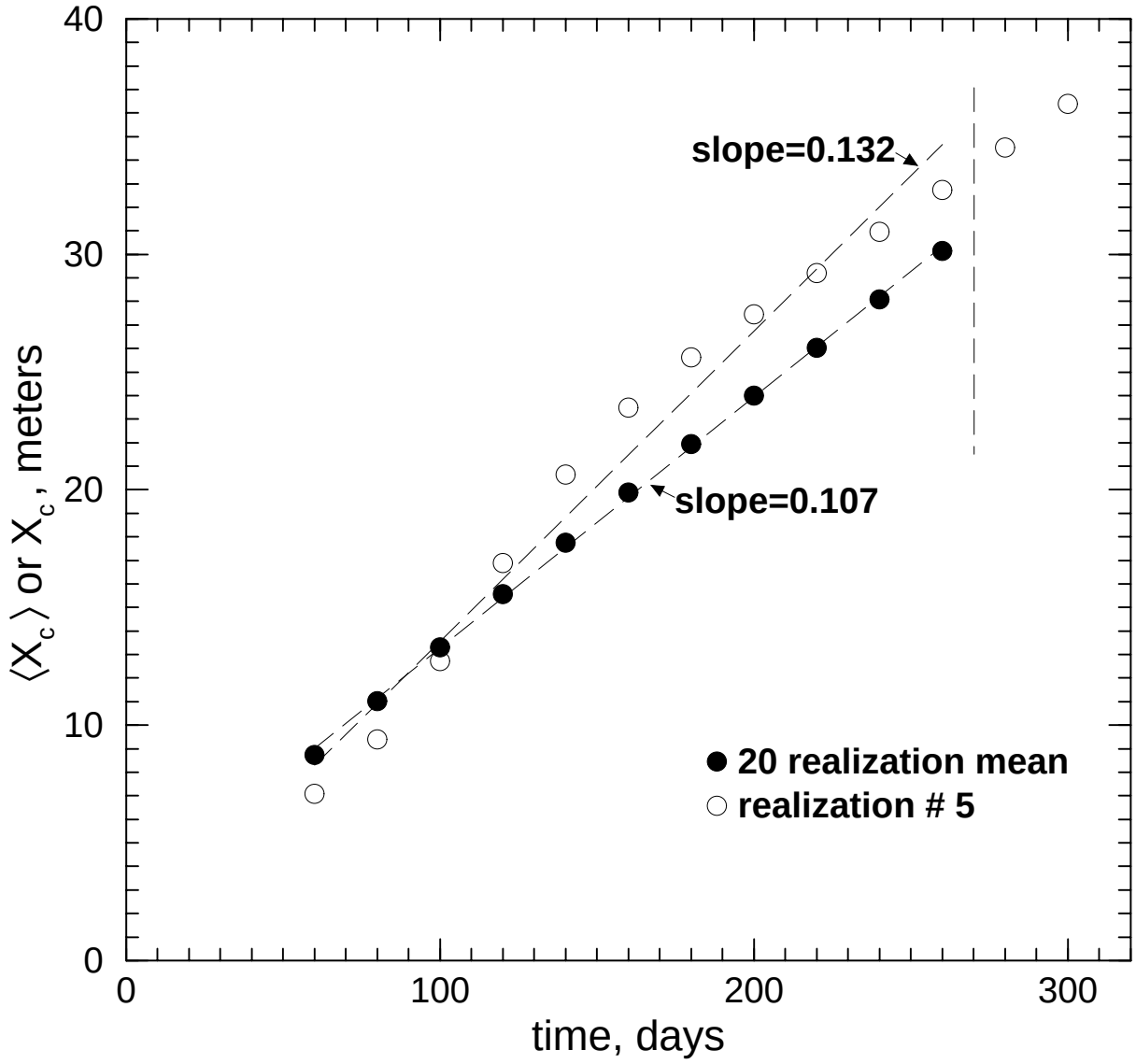
40
30
20
10
0
0
100
200
300
time, days
⟨Xc⟩ or Xc, meters
slope=0.132
slope=0.107
20 realization mean
realization # 5

FIGURE 12

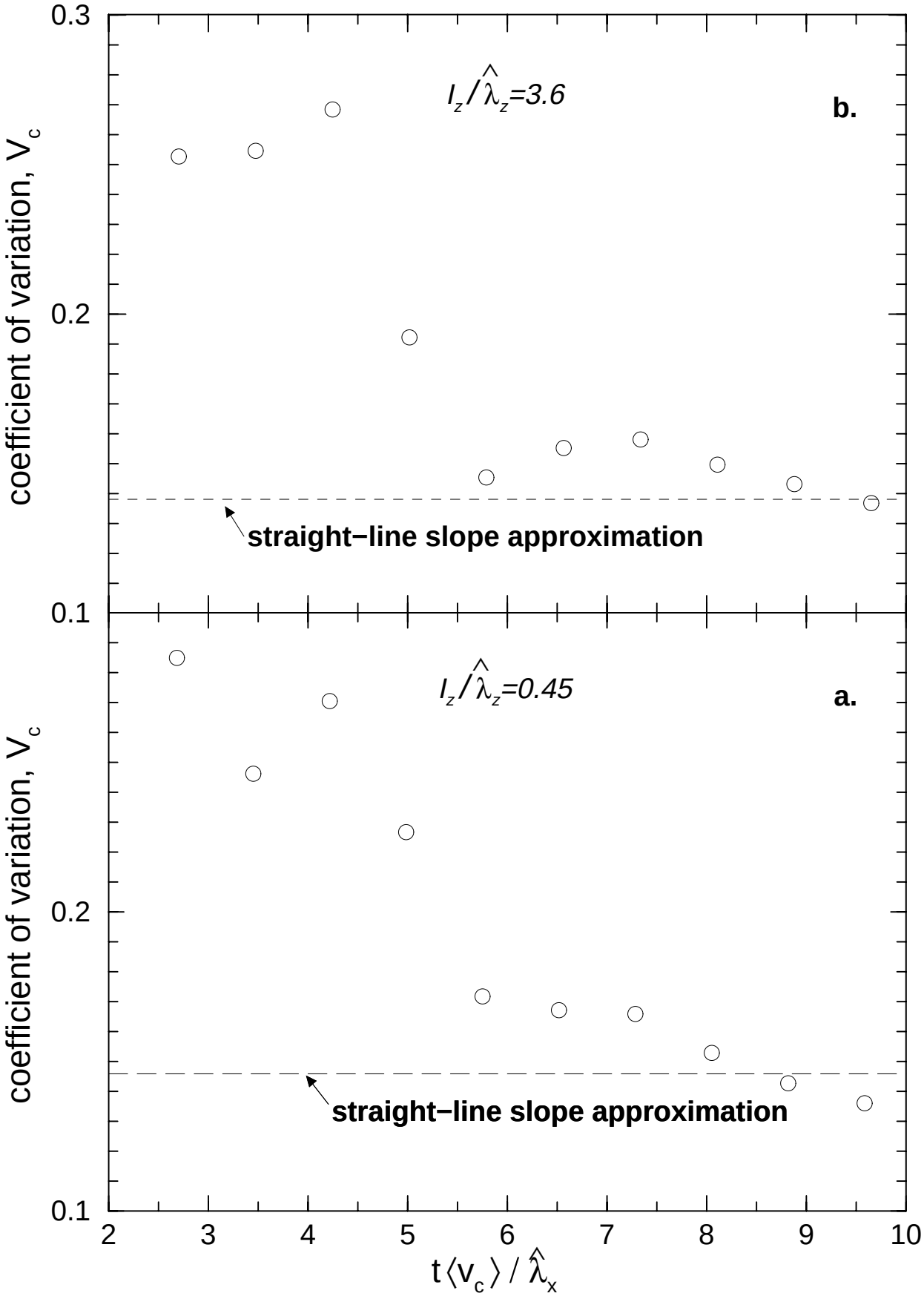
0.3
0.2
0.1
coefficient of variation, V_c
$I_z/\hat{\lambda}_z$=3.6
b.
straight−line slope approximation
$I_z/\hat{\lambda}_z$=0.45
a.
straight−line slope approximation
2
3
4
5
6
7
8
9
10
$t\langle v_c\rangle / \hat{\lambda}_x$

FIGURE 13

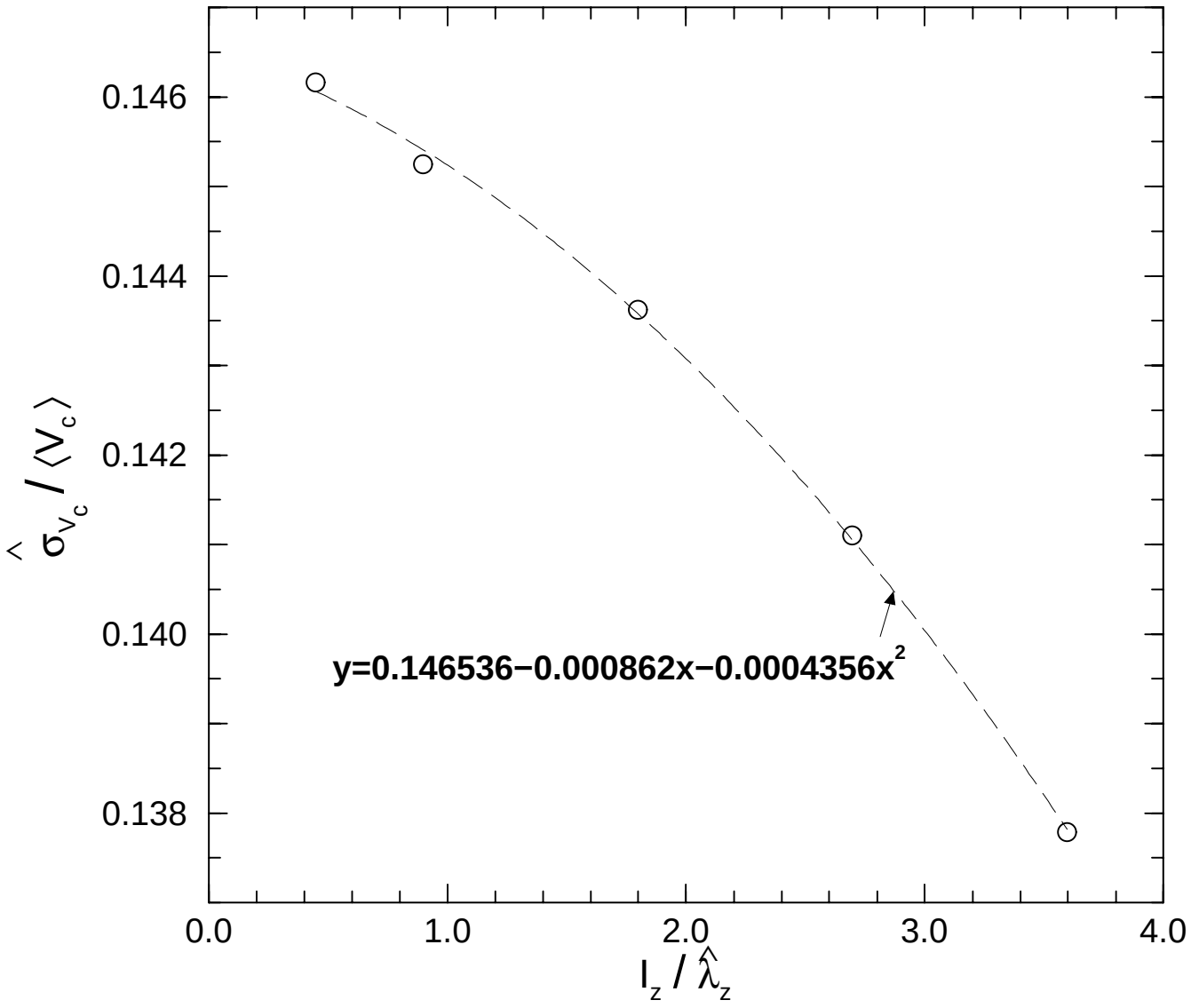
0.146
0.144
0.142
0.140
0.138
0.0
1.0
2.0
3.0
4.0
$\hat{\sigma}_{V_c} / \langle V_c \rangle$
$l_z / \hat{\lambda}_z$
y=0.146536−0.000862x−0.0004356x²

FIGURE 14

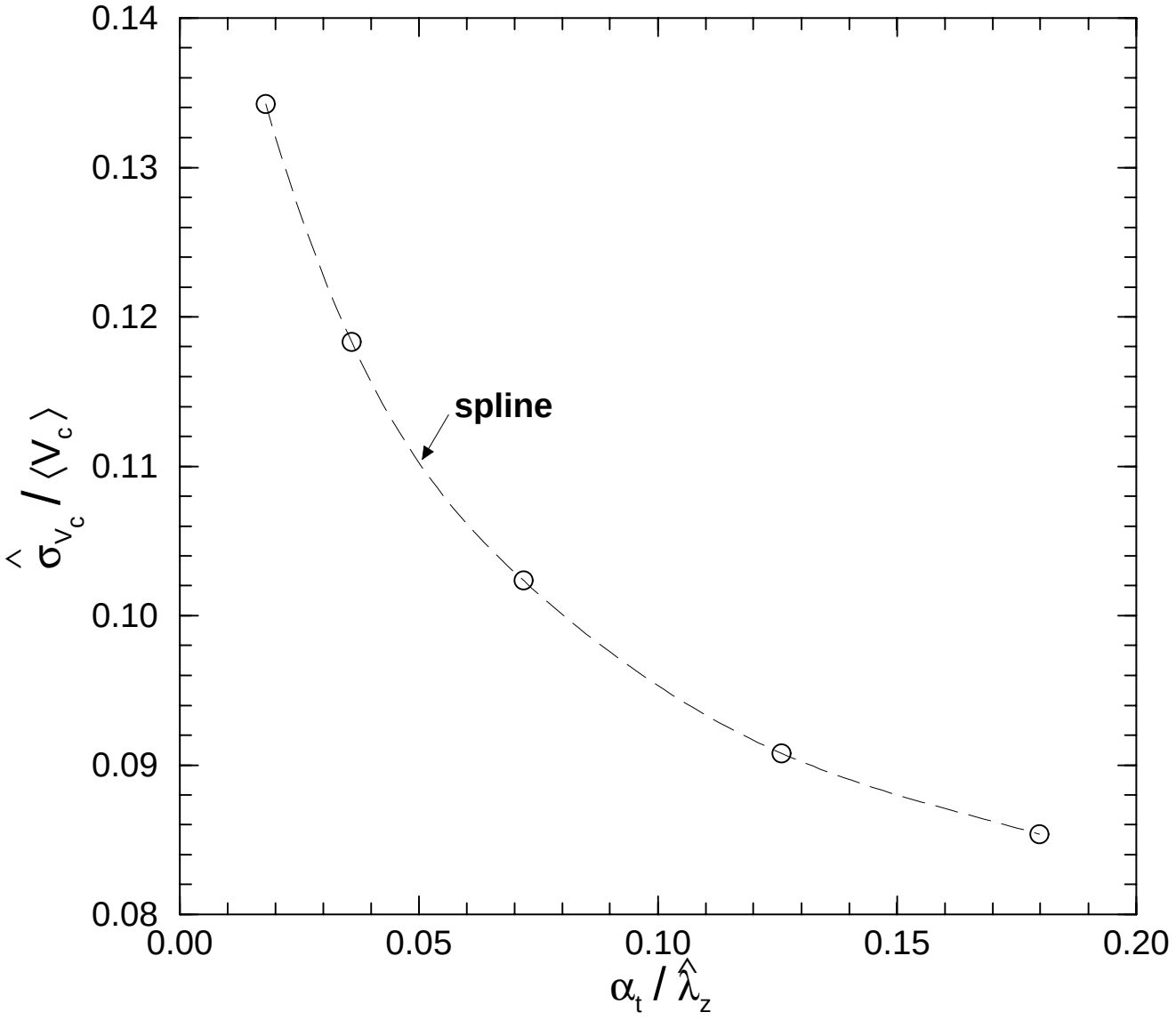
0.14
0.13
0.12
0.11
0.10
0.09
0.08
0.00
0.05
0.10
0.15
0.20
spline
$\hat{\sigma}_{V_c} / \langle V_c \rangle$
$\alpha_t / \hat{\lambda}_z$